Volume 12
Number 17
7 May 2024
Pages 9911–10580

Journal of Materials Chemistry A

Materials for energy and sustainability

rsc.li/materials-a

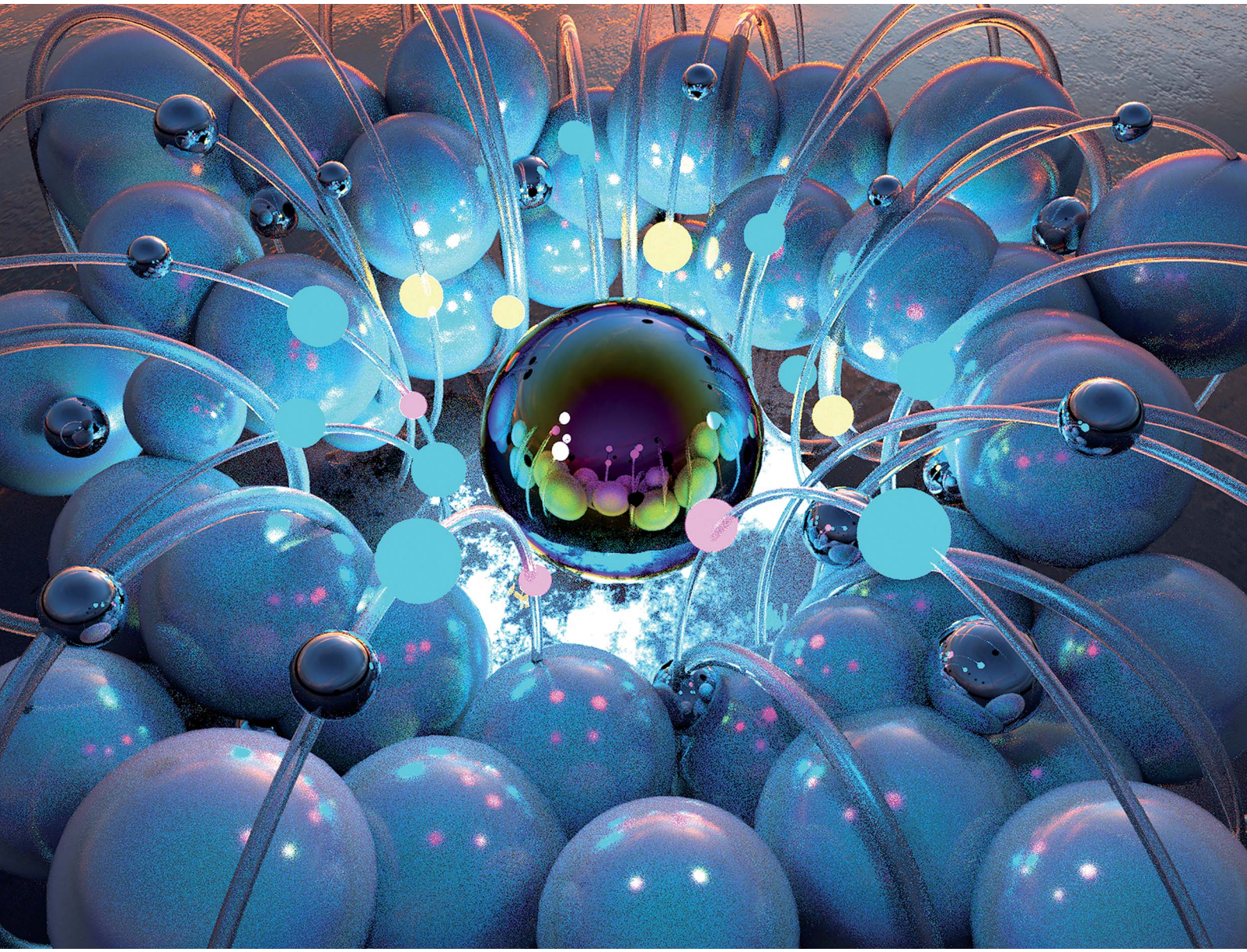

ISSN 2050-7488

ROYAL SOCIETY OF CHEMISTRY

REVIEW ARTICLE

Liang Yu, Wei Yuefan, Huang Yizhong *et al.*

A review of noble metal-free high entropy alloys for water splitting applications

Journal of Materials Chemistry A

REVIEW

View Article Online
View Journal | View Issue

Cite this: J. Mater. Chem. A, 2024, 12, 9933

A review of noble metal-free high entropy alloys for water splitting applications

Hamzah Kamaruddin, †[ca] Zhang Jianghong,†[a] Liang Yu,*[b] Wei Yuefan *[d] and Huang Yizhong *[a]

Nano-sized high entropy alloy (HEA) catalysts have attracted much attention as extraordinary electrocatalysts in water-splitting applications, *i.e.*, the hydrogen evolution reaction (HER) and oxygen evolution reaction (OER). Recently, there has been heightened interest in metal-free HEA catalysts, which are often considered more sustainable than their noble metal counterparts, while still performing competitively. Therefore, updating the current progress of the state-of-the-art electrolysis of HEAs is essential. This review aims to summarize the recent research progress of noble metal-free HEA nanocatalysts and their performances in the HER and OER. The critical concepts of HEAs, recently reported preparation methods and their performances in water-splitting are focused on in this review. This review also provides a perspective on the existing limitations of HEAs and an outlook for research into noble metal-free HEA nanocatalysts for the HER and OER.

Received 30th January 2024
Accepted 20th March 2024

DOI: 10.1039/d4ta00690a

rsc.li/materials-a

[a]School of Materials Science and Engineering, Nanyang Technological University, 50 Nanyang Avenue, Singapore 639798. E-mail: HAMZ0002@e.ntu.edu.sg; m220019@e.ntu.edu.sg; yzhuang@ntu.edu.sg

[b]School of Materials Science and Technology, Shenyang University of Chemical Technology, Shenyang, 110142, Liaoning Province, China. E-mail: liangyuaadd@126.com

[c]Advanced Remanufacturing and Technology Centre (ARTC), Agency for Science, Technology and Research (A*STAR), 3 Cleantech Loop, #01/01 CleanTech Two, Singapore 637143, Republic of Singapore

[d]Singapore Institute of Manufacturing Technology (SIMTech), Agency for Science, Technology and Research (A*STAR), 3 Cleantech Loop, #01/01 CleanTech Two, Singapore 637143, Republic of Singapore. E-mail: wei_yuefan@simtech.a-star.edu.sg

† These authors contributed equally.

1. Introduction

The development of sustainable and efficient electrocatalysts has, in recency, gained much attention with research pivoting towards greater environmentalism amidst impending energy crises. As traditional fuel sources become increasingly unsustainable, newer alternative power sources have emerged. Photocatalysts,[1–6] for example, have risen in popularity in recent years. With the main energy source stemming only from accessible solar energy, photocatalysts are thus considered drivers of cleaner alternative energy, such as hydrogen production *via* water splitting,[7,8] CO_2 reduction,[9,10] and other

Hamzah Kamaruddin

*Hamzah Kamaruddin is a current PhD student at the School of Materials Science and Engineering, Nanyang Technological University under the supervision of Professor Huang Yizhong. After graduating with a first-class honours degree in the same field and school in 2022, he received the prestigious Agency for Science, Technology and Research (A*STAR) Graduate Scholarship and is attached to the Advanced Remanufacturing and Technology Centre (ARTC), A*STAR. His research interests include developing novel high entropy materials for electrocatalysis, electron microscopy techniques and hydrogen fuel cells.*

Zhang Jianghong

Zhang Jianghong received his Bachelor of Engineering degree in New Energy Science and Engineering (2021) from Xiamen University Malaysia and Master of Science degree (2022) from the School of Materials Science and Engineering (MSE), Nanyang Technological University (NTU), Singapore. He is currently a PhD student at the NTU MSE. His current research interests include the development of high-entropy alloy materials and the theoretical study in electrocatalysis.

oxidation reactions,[11] which are highly sought after in the world today. Another class of materials known as electrocatalysts is poised to be at the forefront of newer energy applications, including water-splitting applications, fuel cells and energy storage.[182–185] Essentially, electrocatalysts are materials that take part in electrochemical reactions, such as the evolution of hydrogen and oxygen gases during the water splitting process.[12] In electrocatalysis, a catalyst is often required to drive the reactions involved by introducing different reaction pathways with lower thermodynamic potentials.[13] Traditionally, noble metal-containing catalysts for water splitting, including palladium,[14–16] platinum[17–19] and iridium,[20–22] have dominated the electrocatalyst energy market due to their exceptional electrocatalytic abilities compared to regular metals. A large drawback to having these noble metals, however, is their high cost, scarcity, and susceptibility to corrosion.[23–25] This severely restricts their electrocatalytic capabilities in applications. Tremendous breakthroughs have been achieved in the search for alternative catalytic materials as electrocatalysts that can perform competitively with conventional noble metal catalysts. These novel catalysts are also produced by industry-friendly and sustainable methods. These efforts are pivotal in elevating electrocatalysis, including processes such as hydrogen and oxygen production from water-splitting, a viable alternative to overcome our overreliance on unsustainable energy sources such as coal, oil, and gas.[26–28]

High entropy alloys (HEAs) have surfaced as one of the most promising candidates because of their cost-effectiveness, electrocatalytic abilities, and adjustability. HEAs are a new class of materials typically composed of several elements in near-equimolar or equimolar ratios.[29] Conventionally, HEAs are composed of five or more dissimilar elements that are structurally stable and resistant to degradation due to the maximization of the configurational entropy between the constituents.[29] Consequently, this increased inherent entropy allows HEAs to participate well in electrocatalytic applications such as ammonia oxidation[30] and decomposition,[31–33] carbon monoxide oxidation,[34–36] and water splitting. Other similar high entropy materials, such as high entropy oxides (HEOs)[37–39] and high entropy borides (HEBs)[40–42] are also reported to perform well in water-splitting applications. Specifically, the hydrogen evolution reaction (HER) and oxygen evolution reaction (OER) are the key processes in water splitting to produce hydrogen and oxygen gases respectively. These gases are instrumental for the functions of the proton exchange membrane fuel cell (PEMFC) and other such applications which produce clean energy from these gases, in which HEAs are crucial as catalytic electrodes.[43] However, many of the reported HEAs in recent years still contain noble metal components to enhance the catalytic performance of the HEA catalyst in the HER and OER, which is still detrimental to the overall sustainability of HEAs. Furthermore, existing conventional synthesis methods for HEAs are usually tedious and energy-intensive, which diminishes their adoption in industrial applications compared to conventional noble metal catalysts.

Liang Yu

Dr Yu Liang is currently a lecturer at the Department of the School of Materials Science and Engineering, Shenyang University of Chemical Technology. She obtained her PhD degree in Materials Science from the China University of Geosciences (Beijing) (2016). Her current research interests include development of novel electrocatalysts for water splitting, novel photocatalysts for hydrogen generation and mineral modification.

Wei Yuefan

Dr Wei Yuefan is a senior scientist at the Singapore Institute of Manufacturing Technology (SIMTech) in Singapore. She has published over fifty articles in journals or trend magazines. Her research interests include renewable energy resources and technologies, climate change and greenhouse gas mitigation, energy and sustainable development.

Huang Yizhong

Professor Yizhong Huang is currently positioned in the School of Materials Science and Engineering at Nanyang Technological University in Singapore. He has been working at the University of Oxford as a postdoc, research fellow, college fellow of Wolfson, and an academic visitor. He has published over three hundred and sixty papers in journals such as Nature, Nature Communications, Nano Letters, Advanced Materials, and ACS Nano. He has research interests in nanoelectrochemistry and hybrid nanostructured materials for energy applications. He leads a strong academic group including postdoctoral research fellows, postgraduates and visiting scientists.

Herein, we propose a systematic review of recent noble metal-free HEA catalysts for both HER and OER applications. We first describe the definition of HEAs and then provide a summary of novel synthesis strategies to create HEAs, namely carbothermal shock synthesis, fast-moving bed pyrolysis, laser-based synthesis methods, and dealloying strategies. Subsequently, we present a cost analysis of the conventional metal components used in HEAs. We then present a summary of recent noble metal-free HEAs employed in HER and OER processes respectively, with their catalytic performances listed as well. Structure–property relationships involved in the design of HEAs were analyzed as well. Although there exist many reviews highlighting the synthesis of HEAs for water splitting applications, few to our knowledge have compiled strictly noble metal-free HEA variants for water splitting. This review highlights the various considerations involved in creating noble metal-free HEAs that have been reported to perform excellently when benchmarked with noble metals. Furthermore, we also considered the effect that certain transition metal elements had on the performance. At present, noble metal-free HEAs show immense potential as a sustainable catalyst which, with newer synthesis methods, is also an industry-friendly alternative material compared to existing noble metal catalysts.

2. Definition of high entropy alloys

The thermodynamic properties of HEMs are often studied to elucidate why these materials perform well in energy applications. Since the discovery of HEAs, four governing effects, known as the 'four core effects', have generally been involved when defining HEAs.[44–46] These four effects, namely the high-entropy effect, sluggish diffusion effect, lattice distortion effect, and cocktail effect, are illustrated in Fig. 1. They provide important insights into why high-entropy alloys (HEAs) exhibit electrocatalytic abilities.

The high entropy effect refers to the presence of multiple constituent elements in near-equal or equimolar proportions, which results in high mixing entropy (ΔS_{mix}), affording thermodynamic stability to the HEA system.[47,48] The mixed Gibbs free energy of the entire HEA system can be expressed in eqn (2.1):

$$\Delta G_{\mathrm{mix}} = \Delta H_{\mathrm{mix}} - T\Delta S_{\mathrm{mix}} \quad (2.1)$$

where ΔG_{mix} refers to the mixed Gibbs free energy, ΔH_{mix} refers to the mixing enthalpy, and T refers to the temperature of the system.[46] A negative value of ΔG_{mix} indicates that the system spontaneously favours the creation of a single-phased HEA state, while a positive value indicates the tendency for phase

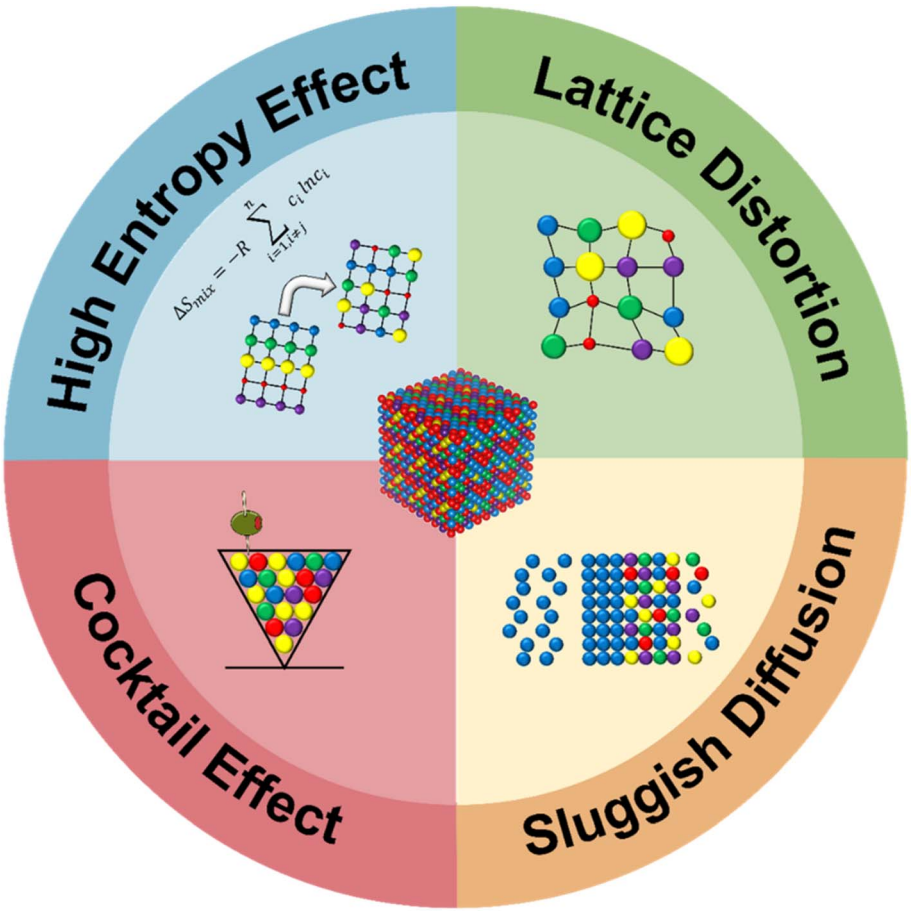

Fig. 1 Schematic diagram of the 'four core effects' of HEAs.

separation to occur. When ΔS_{mix} surpasses the ΔH_{mix} of the system, the system tends to form a solid solution and become thermodynamically stable. Recent studies have exploited the high entropy effect of HEAs for use in various mechanical,[49–51] catalytic,[52–54] and even biomedical applications.[55–57] Lei *et al.*[58] for example used the high entropy effect of Si-based high entropy anode materials synthesized *via* ball milling and found that the material performed well as an anode for lithium-ion batteries which was able to undergo reversible structural changes during cycling, leading to its overall cycling stability.

The random distribution of metal atoms in HEAs results in complex and higher mixing entropy compared to regular alloy systems, consequently leading to reduced diffusivity. Since higher energy is required to trigger the diffusion of metal atoms, the HEA system becomes more stable with a decrease in the diffusion rate of the atoms. This is known as the sluggish diffusion effect.[46] Several studies have previously conducted secondary observations on the formation behaviour of nanocrystals and amorphous phases during solidification.[59–61] Tsai *et al.*,[62] for instance, found that CoCrFeMnNi HEA displayed sluggish diffusion behavior and found that the diffusion coefficients of HEA were lower than those reported in established references.

The cocktail effect refers to the synergistic combination of multiple constituent metal atoms within the HEA that contributes to the overall properties of the material. Although the exact mechanism for this synergistic effect remains largely unknown, the cocktail effect is essential for HEAs to achieve desired properties in terms of high strength, hardness, corrosion resistance and electrocatalytic abilities.[46,63–65] Often, unexpected synergies between constituent elements induce exemplary performances in different applications which is largely unpredictable. A roadblock to fully understanding the mechanisms behind the cocktail effect lies within the large variety of active sites that HEAs may possess which complicates existing mechanistic models, for example the Sabatier volcano plot which does not consider the contributions of active sites and the limitation of a linear scaling relation.[66,67] Efforts have been made to establish newer models that account for these various factors. Chen *et al.*,[68] for example, recently reported their new quantitative model to establish relationships between the adsorption energy distribution in HEAs and the cocktail effect. However, more in-depth analyses are required in this aspect of the understanding of HEAs to fully understand cocktail effect mechanisms.

The difference in sizes between constituent metal atoms in HEAs creates a disorderly arrangement of atoms due to the shifting of atoms from their ideal atomic locations in the atomic lattice.[46] This results in severe distortion of the lattice due to size mismatches[69] and results in surface strain which contributes to configurational entropy.[70] Consequently, this affords HEAs with excellent mechanical properties such as high yield strength and ductility,[71–73] as well as good catalytic properties,[74–76] although the effect on mechanical properties is more widely reported. Li *et al.*[77] found that the selective laser melting of CoCrFeMnNi HEA displayed large numbers of dislocations and severe lattice distortion. Interestingly, the authors observed nanotwins and tetragonal phases which had never been observed prior to this. The authors reported that the presence of these tetragonal phases and ultrafine grains improved the mechanical properties of the synthesized HEA.

Overall, a keen understanding of the 'four core effects' is crucial to improving the quality of HEAs for various applications. A common problem with the design of noble metal-free HEAs today is a current lack of understanding of the various considerations including these 'four core effects'. Thus, the inclusion of noble metals with better inherent catalytic abilities is often included to improve the performance of these noble metal-free HEAs. This poses a major sustainability and economic problem in the HEA industry as we explain in the following section. Apart from including these noble metals as a potential solution, the need for more facile synthesis methods, studies involving the effect of transition metal elements as catalytic enhancers, and a concrete understanding of thermodynamic optimizations with the help of simulations and first-principle calculations can improve both the performance of noble metal-free HEAs and also their adoption in industry.

3. Cost analysis of noble metals in electrocatalysis

Much research has been performed on the synthesis of nanoscale HEA materials in both noble and noble-free systems. In the context of HEAs, the creation of active surface sites *via* the combination of metal atoms is instrumental in electrocatalysis.[78] The unique binding interactions between the metal atoms can create active surface sites that facilitate effective bonding and anti-bonding of adsorbates in water-splitting applications such as the HER and OER, respectively.[79–81] In nanoscale noble metal systems, metals such as platinum display exceptional properties in the HER due to its inherent (111) face-centered cubic (FCC) crystal structure with edge sites as active sites.[43,82] Contrastingly, in noble-free systems, the primary mechanism for these systems to compete energetically with noble metal systems is to influence the d-band centers to regulate the surface strain and electronic structures of these HEA systems.[83,84]

The majority of the reported HEA nanocatalysts contain noble metals to improve their catalytic properties. However, compared to non-noble metals, noble metals such as platinum (Pt), iridium (Ir), and ruthenium (Ru), are far less abundant. As listed in Table 1, Pt, Ir and Ru only take up $\sim 10^{-7}$% of the earth's crust. Their scarcity not only results in their high cost (*e.g.* Pt \$28 800 000/T and Pd \$38 400 000/T), but also raises concerns about the sustainability of their supply for widespread application. Besides, the mining and refining of noble metals have significant environmental impacts. All these factors restrict the large-scale production of noble metals, while non-noble metals, including Fe (5.63%), Mg (2.33%), Co (2.5×10^{-3}%) and Ni (8.4×10^{-3}%), are comparatively more abundant and cost-effective (*e.g.* iron ore \$120/T and Co \$33 420/T), making them appealing for commercial purposes.

Table 1 Abundance and price of metal elements

Element	Abundance (%)[a]	Price (USD/T)[b]
Pt	5×10^{-7}	~28 800 000 (~900/t.oz)
Pd	1.5×10^{-6}	~38 400 000 (~1200/t.oz)
Ru	1×10^{-7}	~14 400 000 (~450/t.oz)
Ir	1×10^{-7}	~152 000 000 (~4750/t.oz)
Fe (63.5% Fe-content iron ore)	5.63	~120
Co	2.5×10^{-3}	~33 420
Ni	8.4×10^{-3}	~18 440
Mn	9.5×10^{-2}	~1800
Mg	2.33	~3600

[a] The elemental percentage in earth's crust. [b] The abundance information source;[87] the main price information source: **https://tradingeconomics.com**.

Furthermore, some noble metals are susceptible to corrosion, thus decreasing their long-term value as durable nanocatalysts.[85,86] Noble metal-free HEA nanocatalysts pose as up-and-coming greener and cheaper materials that have the potential to eventually replace the use of noble metal components. Therefore, selecting non-noble metal elements for HEA catalysts has become a significant area of interest in the field of renewable energy.

4. Structure–property relationships & design considerations

Given the critical importance of site-specific characteristics, understanding the relationships between structure and electrocatalytic performance is essential for the development of high-performance HEA catalysts with distinct physical and chemical properties. In this context, the properties of HEAs, *e.g.*, components, composition, and crystal structures, are key factors that need to be considered.

4.1. Factors affecting phase formation

Although the entropy-driven effect theoretically promotes the formation of solid solution, multi-element systems with high mixing entropy do not always form a single crystalline solid solution phase. Hence, the mixing entropy is reckoned to be not the only determining factor for the solid solution or the amorphous phase. In this case, previous studies[88–91] have proposed five parameters to predict the phase formation of multi-element alloys: mixing entropy (ΔS_{mix}), atom radius difference (δ), mixing enthalpy (ΔH_{mix}), electronegativity ($\Delta\chi$) and valence electron concentration (VEC).

4.1.1. Mixing entropy (ΔS_{mix}). The disorderliness of the system when different elemental atoms are combined is called mixing entropy. It quantifies the configurational possibilities of atom arrangements as multiple elements are mixed.

$$\Delta S_{\mathrm{mix}} = -R \sum_{i=1,i\neq j}^{n} c_i \ln c_i \tag{4.1}$$

where R is the gas constant (8.314 J mol^{-1} K^{-1}).

4.1.2. Atomic radius (δ). The variation in atomic radii among the constituent elements in the alloy systems is given by:

$$\delta = 100\sqrt{\sum_{i=1}^{n} c_i\left(1-\frac{r_i}{\bar{r}}\right)^2} \tag{4.2}$$

where $\bar{r} = \sum_{i=1}^{n} c_i r_i$, c_i and r_i are the atomic percentage and atomic radius of the ith element.

4.1.3. Mixing enthalpy (ΔH_{mix}). The change of energy associated with the mixing of different elements for alloy formation is called mixing enthalpy. It indicates the degree of atomic–level interactions between the constituent elements.

$$\Delta H_{\mathrm{mix}} = \sum_{i=1,i\neq j}^{n} \Omega_{ij} c_i c_j \tag{4.3}$$

where $\Omega_{ij} = 4\Delta_{\mathrm{mix}}^{\mathrm{AB}}$, $\Delta_{\mathrm{mix}}^{\mathrm{AB}}$ is the mixing enthalpy of binary liquid AB alloys.

4.1.4. Electronegativity difference ($\Delta\chi$). The variation in electronegativity among the constituent elements is the electronegativity difference. It can affect the distribution of electrons and thus the adsorption energy of catalytic intermediates on HEAs.

$$\Delta\chi = \sqrt{\sum_{i=1}^{n} c_i(\chi_i - \bar{\chi})^2} \tag{4.4}$$

where $\bar{\chi} = \sum_{i=1}^{n} c_i\chi_i$, χ_i is the Pauling electronegativity for the ith element.

4.1.5. Valence electron concentration (VEC). VEC is the concentration of valence electrons within the material, which influences the phase stability of the alloy. Here, valence electrons are the electrons in the outermost energy level of an atom, determining the chemical properties and the interactions with other atoms. It should be mentioned that VEC is different from e/a (the average number of itinerant electrons per atom).

$$\mathrm{VEC} = \sum_{i=1}^{n} c_i(\mathrm{VEC})_i \tag{4.5}$$

where $(\mathrm{VEC})_i$ is the VEC for the ith element.

Guo *et al.*[88] established criteria for solid solution formation in HEAs with specifying ranges: $0 \le \delta \le 8.5$, $-22 \le \Delta H_{\mathrm{mix}} \le 7$ kJ mol^{-1}, and $0 \le \Delta S_{\mathrm{mix}} \le 8.5$ J (K^{-1} mol^{-1}) or $11 \le \Delta S_{\mathrm{mix}} \le 19.5$ J (K^{-1} mol^{-1}). In contrast, amorphous phases are likely to form under conditions of more negative mixing enthalpy, larger

atomic size differences and different mixing entropy ranges ($\delta \geq 9$, $-49 \leq \Delta H\_mix \leq 5.5$ kJ mol^{-1}, $7 \leq \Delta S\_mix \leq 16$ J (K^{-1} mol^{-1})). $\Delta\chi$ shows no significant effect on phase formation. VEC also lacks controlling influence on phase formation and stability, whereas it critically influences the types of crystal structures of solid solution. It is suggested that VEC ≥ 8 and $5 <$ VEC < 6.87 favor FCC and BCC structures, respectively, while VEC between these values showed mixed FCC + BCC structures.[90,91]

Alternatively, DFT (density functional theory) computation has been employed to estimate the Gibbs free energy of formation and formation temperature ($\Delta G_{mix} = \Delta H_{formation} - T\Delta S_{mix}$) of HEA solid solution.[92] Eqn (4.6) describes the formation of a quinary alloy (5 elements) and the enthalpy of formation ($\Delta H_{formation}$) refers to the difference in calculated DFT energy between the alloy system ($A_xB_yC_zD_pE_q$) and pure metals (A, B, C, D and E). Thermodynamically, ΔH_{mix} acts as the barrier for the formation while the entropy-driven effect ($-T\Delta S_{mix}$) provides promotion, especially at sufficiently high temperature. In this method, the vibrational energy and surface-energy effects of nanoparticles are ignored, and the real entropy is higher than the estimated entropy due to the short-range ordering. Thus, the predicted formation temperature only represents the lower limit.

$$xA + yB + zC + pD + qE \rightarrow A_xB_yC_zD_pE_q \quad (4.6)$$

in which A, B, C, D and E represent five types of metal elements and x, y, z, p and q ($x + y + z + p + q = 1$) are the compositions of each element.

4.2. Element selection

The rational selection of elements also plays a vital role in the improvement of catalytic performance. Engineering of element configurations and compositions can well tailor the active sites. Normally, the selection of elements is dependent on target reactions. For example, the noble metals Ru, Ir and Pt usually serve as active sites in the HER and OER.[21,78,93,94] Fig. 2 exhibits the frequency of non-noble metal element selection for the application of water electrolysis. 3d transition metals, particularly Ni, Fe, Co, Mn, Cr and Cu, are most commonly utilized. In the presence of noble metals, element selection is usually associated with ligand effects on these active sites. In contrast, in the design of non-noble metal catalysts, the tuning of overall electronic structures (*e.g.*, d-band centers and charge distribution) is of importance, which influences the interactions with reactants and catalytic intermediates. These electronic properties can be adjusted through rational element selection. Besides, multiple active sites are formed in HEAs, resulting from the arrangements of multi-elements adjacent to each other. The various adsorption energies on these multiple active sites form a continuous spectrum, that is, the adsorption energy distribution curve. By fine-tuning the elemental components and compositions, this curve can be optimized for desired adsorption energy in target reactions. Crucially, it is the properties of individual elements that determine the behavior of their alloy systems. The differences in electronegativity of adjacent atoms will affect the charge distribution and thus the adsorption energy. Besides, valence electrons also have an influence on the adsorption strength of specific intermediates, thus enhancing the reaction process.

4.3. Crystal phases and stability

The atoms of multiple principal elements in HEAs are often organized into solid solutions with body-centered cubic (BCC), face-centered cubic (FCC), and hexagonal close-packed (HCP). The four core effects of HEAs (high-entropy effect, sluggish diffusion effect, lattice distortion effect and cocktail effect), especially the high-entropy effect, contribute to the formation of the solid solution. So far, the majority of HEA NPs reported for

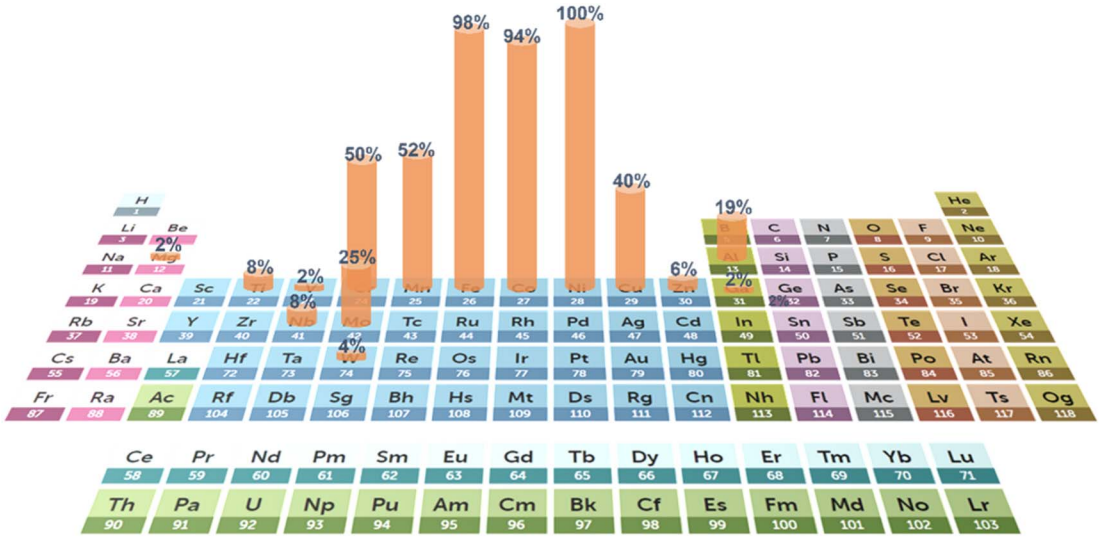

Fig. 2 Addition frequency of various elements of HEAs for HER and OER electrocatalysts from recent research. (The periodic table is from the Royal Society of Chemistry[107]).

Table 2 Synthesis methods of noble metal-free HEAs with the respective crystal structures and catalytic applications

Material	Synthetic method	Crystal structure	Catalytic reaction	Reference
MnFeCoNiCu	Solvothermal	FCC	OER	96
FeNiMnCrCu and FeCoNiCrAl	Arc melting	FCC + BCC (binary)	OER	84
NiFeMoCoCr	Arc-melting	FCC or FCC + μ	HER	99
CuAlNiMoFe	Arc-melting	BCC	HER	125
FeCoNiMnMg	Carbothermal shock synthesis	—	Supercapacitor	126
CoMoFeNiCu	Carbothermal shock	FCC	NH_3 decomposition	31
CoCrFeMnNi	Laser ablation	FCC	OER	106
CrCoFeNiMn and CrCoFeNiMnMo	Pulsed laser ablation	Amorphous	OER	127
CrMnFeCoNi	Pulsed laser deposition	—	OER	109
AlCrFeCoNiCu	Pulsed laser deposition	FCC + BCC	—	108
FeCoNiCu	Pulsed laser irradiation	FCC	OER and HER	115
FeCoNiCrNb	Dealloying	Laves phase	OER	128
AlNiCoFeX (X = Mo, Nb, and Cr)	Dealloying	FCC + spinel (binary)	OER or ORR	129 and 130
FeCoNiAlTi	Dealloying	L_{12}-type intermetallics	HER	131
NiFeCoCuTi	Alloying/dealloying	FCC	HER	132
FeCoNiWMo	Mechanical alloying	FCC + rhombohedral (binary)	HER	133
CrMnFeCoNi	Sputtering	Amorphous	ORR	134
CrMnFeCoNi	Sputtering	FCC, BCC and amorphous	ORR	135
CoCrFeNiMo	Microwave sinter	FCC	OER	136
V_xFeCoNiCuMn (x = 0, 0.5, and 1.0)	High-energy ball-milling	FCC	HER	137
Cr_xMnFeNi (x = 0.8, 1.0, 1.5)	Vacuum induction melting	FCC and BCC	OER and HER	95
NiCoFeMoMn	Arc melting, single-roller melt spinning and dealloying	FCC	OER and HER	138
TiCrMnFeCoNiZrNbMo	Arc melting	FCC + BCC	OER and HER	100

water-splitting are FCC and BCC, as shown in Table 2. Firstly, the exhibitions of these structures may result from the VEC of frequently utilized elements (Cr (6), Mn (7), Fe (8), Co (9), Ni (10), and Cu (11)). According to the VEC criteria (Section 4.1), alloys consisting of these elements usually have VEC within the specified range (VEC $\geq$ 8 and 5 < VEC < 6.87), which the FCC and BCC phases favor. Secondly, these structures are energetically favored and thus demonstrate thermodynamic stability, making them common choices in alloy formation. Additionally, FCC and BCC structures offer flexibility in accommodating a wide range of elements and compositions. HEAs are characterized by their diverse elemental combination; thus, these structures readily accommodate these diverse sets of elements without phase separation. The crystal structures vary with the element compositions. Wang *et al.*[95] transformed the FCC of Cr_xMnFeNi into the BCC-prominent phase by increasing the Cr content. Lattice distortion also enhances the incorporation of multiple elements into a solid solution. It accounts for the crystal structure of HEAs with defects, which are usually found during material characterization. These imperfections can improve catalytic activity by providing more active sites. Huang *et al.*[96] reported defects in MnFeCoNiCu HEAs. TEM fast Fourier transform analysis demonstrates the presence of stack faults and dislocation in the nanoparticles. It is speculated that these defects increase the surface energy, facilitating the OER catalytic reaction more efficiently. It needs to be mentioned that the misfit of the atom radius will lead to amorphous or even phase-segregated structures. For example, yttrium and lanthanide elements were reported to enable the formation of metallic glass, in which further large atom sizes destabilize the crystal structures and collapse the crystal structure.[97,98]

In general, HEAs exhibit excellent thermal stability and corrosion resistance. At sufficiently high temperature, HEAs with large mixing entropy ΔS_{mix} make the mixing Gibbs energy more negative, increasing the solubility limit of the element in the alloy system. Thus, phase transformation can be suppressed and stable structures can be formed. In addition, the presence of a single-phase accounts for the excellent corrosion resistance of HEAs. The homogeneous phase structure eliminates the presence of galvanic cells within the material, which are often responsible for localized corrosion processes such as pitting, crevice corrosion and galvanic corrosion. Essentially, without significant phase segregation, there are fewer "weak spots" for corrosion to initiate. Multiple phases in an alloy would lead to the presence of phase boundaries, which are preferred sites for corrosion initiation. In contrast, these internal boundaries are seldom observed in the single-phase solid solution; thus, these phases are fewer vulnerable sites to attack by corrosive agents. For example, Zhang *et al.*[99] found that the HEA NiFeMoCoCr with a single FCC structure has higher corrosion resistance than dual phases (FCC + μ) under both acidic and alkaline conditions. Single-phase HEAs exhibit particular randomly disordered chemical elements. The formation of electronegativity among the neighboring elements mitigates the loss of electrons making HEAs less susceptible to corrosion processes. Lattice distortion brings about large surface tension which facilitates the formation of oxides covering the surface of HEAs. These formed oxides generally present a spinal lattice structure contributing to the stabilization of HEAs. In addition, lattice

distortion can also disrupt lattice uniformity, providing protection layers and making corrosion more difficult to occur.[186] Compared to noble metal catalysts, noble metal-free HEAs are susceptible to corrosion, since the half-filled d-orbital of transition metals makes them easy to dissolve. To utilize non-noble HEAs in harsh environments, appropriate approaches should be developed to alleviate corrosion. Tajuddin *et al.*[100] incorporated Nb, Zr, Mo, and Ti into Cr, Co, Ni, Mn, and Fe to enhance the corrosion-resisting ability, in which the formation of the passivation layer by passivation elements (Ti, Zr, Nb, and Mo) prevents HEAs from degradation.

4.4. The influence of noble-metal free HEA design on properties

Generally, the design of HEAs is vital in shaping their electronic and surface properties, thereby influencing their catalytic efficiency. Fig. 3 elucidates how the designs of HEA affect the catalytic performances. The structures and element selections of HEAs can modify the electronic structures, including the d-band center and Fermi energy level. Moreover, the electronegativity difference among the different elements leads to charge redistributions. The redistribution will also influence the electronic density at the surfaces, which is crucial for catalytic activity. Therefore, these properties affect the adsorbate–catalyst interactions. Such interactions are fundamental in determining the adsorption free energy of catalytic intermediates, thus, influencing the overall catalytic performances of HEAs. The insights gained from measuring catalytic performance can then inform and refine initial design strategies, creating a feedback loop that enhances the development and optimization of HEAs.

5. Novel synthesis methods of HEA nanocatalysts

Since the discovery of HEA materials in 2004 by Cantor *et al.*[101] and Yeh *et al.*,[45] a great number of synthesis methods have emerged from the crucial understanding of the four 'core effects' to create HEA catalysts at the nanoscale. Unsurprisingly, many noble metal constituents are often included in the composition of the HEA to enhance its catalytic performance. However, with the advent of newer synthesis methods, researchers have demonstrated that the use of novel and more facile methods of creating noble metal-free HEAs is advantageous for these materials in terms of sustainability and industry-friendliness. Furthermore, several studies, as described in this section, have reported that noble metal-free HEAs can perform as competitively as their noble metal counterparts. This places critical importance on the synthesis method which greatly influences the eventual performance of the noble metal-free HEA product. Fig. 4 gives an overview of the synthesis methods described in this review. While several synthesis methods have been used for noble metal-containing HEAs, these methods can be extended to include noble metal-free variants.

5.1. Carbothermal shock synthesis

A recent popular technique to synthesize HEA nanoparticles (HEA NPs) is the carbothermal shock synthesis (CTS) method proposed by Yao *et al.* in 2018.[102] CTS has been established as an extremely facile method to create multi-component HEAs with excellent performance in water splitting applications. The

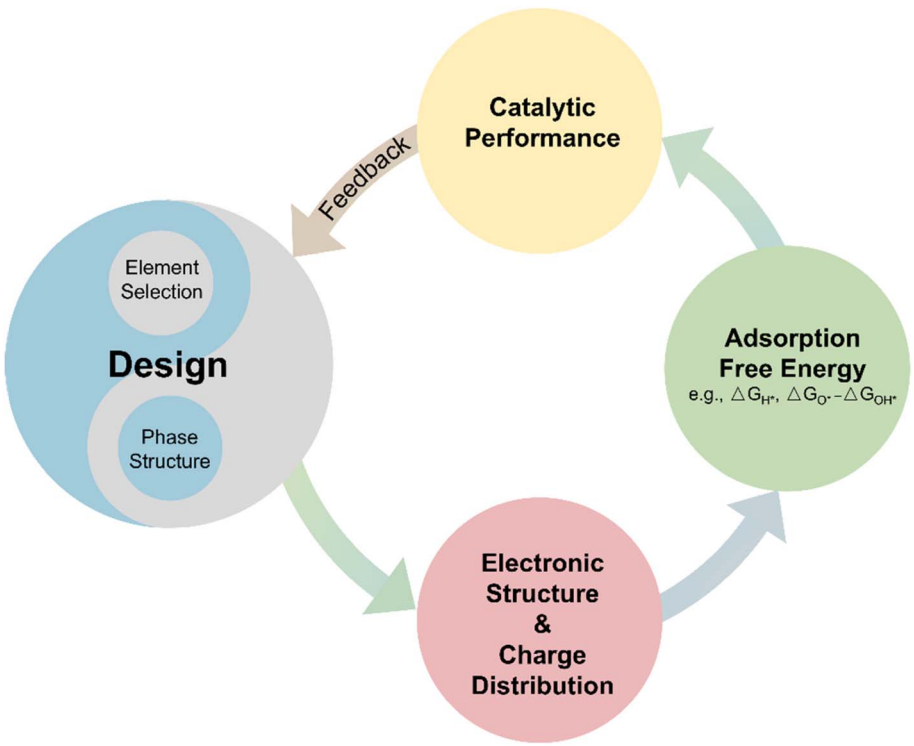

Fig. 3 Relationship between element selection and phase structure and catalytic performance.

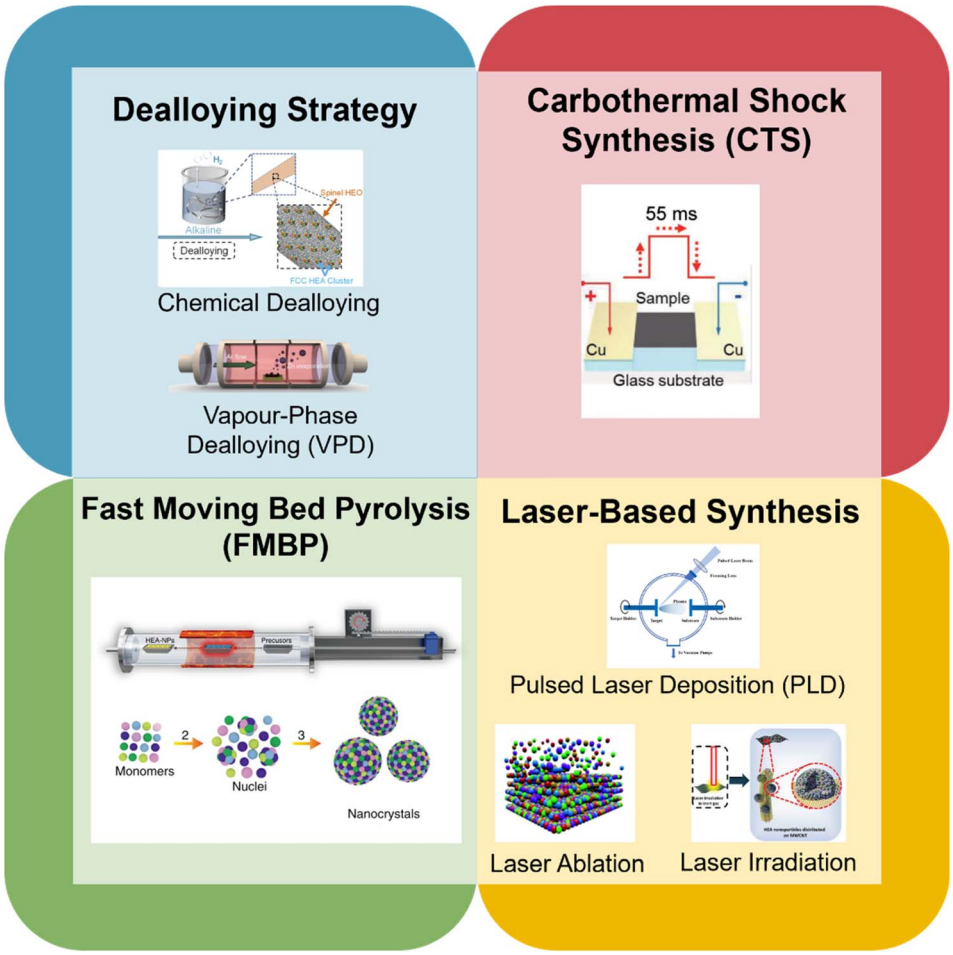

Fig. 4 Overview of novel synthesis methods for HEAs. Reproduced with permission.[120] Copyright Royal Society of Chemistry 2022; reproduced with permission.[124] Copyright Wiley-VCH GmbH 2023; reproduced with permission.[102] Copyright American Association for the Advancement of Science 2018; reproduced with permission Copyright Springer Nature 2020; reproduced with permission.[109] Copyright Elsevier 2022; reproduced with permission.[106] Copyright Royal Society of Chemistry 2019; reproduced with permission.[115] Copyright Wiley-VCH GmbH 2022.

process essentially involved the rapid thermal heating of metal salt precursors loaded onto carbon supports at extreme temperatures (~2000 K). The duration of heating was reported to be around 55 milliseconds, as shown in Fig. 5(a) and such intense thermal shock resulted in the metal salt precursor mixture to undergo rapid phase transformations and chemical reactions. This allowed for the synthesis of single-phased HEA NPs as the rapidity of the process prevented phase separation and the creation of secondary phases, as evidenced in Fig. 5(b) and (c). An advantage of employing such a method is the accessibility of creating quinary, senary, septenary and even octonary HEA NPs, as shown in Fig. 5(c), without the risk of phase separation. Furthermore, the synthesized nanoparticles displayed uniform morphology and sizes (~5 nm) regardless of the HEA composition. This enhanced the electrocatalytic abilities of the HEA nanoparticles through achieving a highly active sites per mass ratio *via* the formation of smaller, multicomponent particles. The authors[102] reported the exemplary performance of 100% ammonia conversion and a markedly high selectivity (>99%) towards the NO_x reaction (NO + NO_2) with a quinary PtPdRhRuCe HEA synthesized using CTS. However, it should be noted that the use of conductive supports, such as the conductive carbon supports employed in this study, was required to facilitate Joule heating in the CTS process.

A more recent study by Abdelhafiz *et al.*[103] reported the synthesis of senary FeNiCoCrMnV noble metal-free HEO nanoparticles using the CTS method. In this study, a remarkably low overpotential of only 220 mV was required to achieve a current density of 10 mA cm^{-2} towards the OER. Comparatively, the electrochemical performance of FeNiCoCrMnV far surpassed that of an IrO_2 noble metal catalyst which produced an overpotential of 320 mV to achieve the same current density. It was also reported that the sizes of the particles were approximately 10 nm which supports the evidence that the working mechanisms of CTS can allow for the creation of smaller sized particles. Furthermore, the HEA NPs were shown to be robust enough to withstand durability testing, displaying sustained electrochemical performance despite 20–90 hours of stability testing.

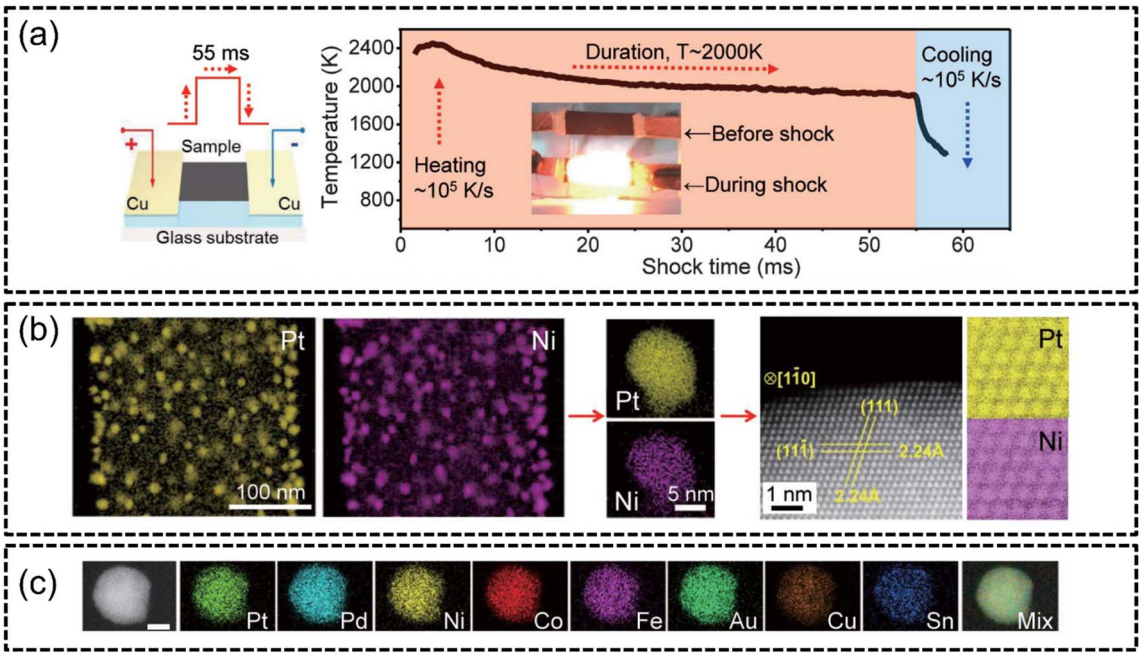

Fig. 5 HEA synthesis *via* CTS from the work of Yao *et al.*, (a) schematic of the CTS and the temperature–time graph of the 55 millisecond shock, (b) STEM-EDX elemental mappings of binary PtNi at low-magnification followed by high-magnification mappings of single particles and HAADF analysis of the atomic arrangement of the alloy, and (c) STEM-EDX elemental mappings of septenary PtPdCoNiFeCuAu. The scale bar is 10 nm. Reproduced with permission.[102] Copyright 2018, American Association for the Advancement of Science.

Apart from the versatility and rapidity of the CTS process, precise control on process parameters such as heating temperature and time can be exploited to tailor the properties of dense nanoparticles' structures. This aspect is crucial for electrocatalytic applications as the density of surface nanoparticles influences the catalytic abilities of the material. Song *et al.*[104] reported the creation of both high density $CuCl_2$-coated cellulose and polyelemental CuPdPtNi NPs using CTS. The surface coverage was reported to be ~85% with very uniform and well dispersed particles. The use of CTS is instrumental in quick heating for carbonization of cellulose to occur through heat transfer from carbon paper supports. This simultaneously synthesized $CuCl_2$ and CuPdPtNi NPs on granular supports. When employed in the CO_2 reduction reaction, the synthesized NPs displayed a good selectivity of around 49% and a sufficient catalytic stability for over 30 hours.

The CTS method has a unique advantage in enabling the creation of multi-metallic HEA NPs since the high temperatures of the process can facilitate the formation of an entropy-stabilized solid solution between different elements, surpassing the past limitation of metallic component immiscibility with respect to one another. A much better control on the size and uniformity of the HEA NPs can also be achieved using CTS. Furthermore, the catalytic activity of noble metal-free HEAs can be greatly improved through the incorporation of more elements in HEAs through this method. However, such a technique requires tremendous amounts of energy to achieve high temperatures in such a short duration. Furthermore, HEA NPs can only be synthesized on conductive supports (such as carbon-based substrates).

5.2. Fast-moving bed pyrolysis

The fast-moving bed pyrolysis (FMBP) established by Gao *et al.* in 2020 (ref. [105]) builds upon the fundamentals of CTS to synthesize HEA NPs on granular supports. Similar to CTS, precursors containing mixed metal salts are quickly pyrolyzed at extreme temperatures to create uniform and well dispersed nano-sized HEA NPs.

An advantage of FMBP is that the need for conductive supports, as in CTS, is circumvented and the ability to create HEAs with many elemental components is possible while also being extremely facile. Gao *et al.* reported that the FMBP method facilitated temperatures of 923 K within 5 s in a vacuum furnace, as depicted in Fig. 6(a), which resulted in the formation of single-phased quinary, senary, septenary and octonary HEA NPs. The successful formation of denary MnCoNiCuRhPdSnIrPtAu HEA NPs of around 50 nm was achieved using this synthesis method. Expanding upon the range of acceptable supports for the system, the authors loaded the HEA NPs onto granular supports such as carbon black, graphene oxide, γ-Al_2O_3 and zeolite, as shown in Fig. 6(b). In the mechanism for the formation of HEA NPs using FMBP, the authors explained that there is a strong correlation between the free energy of nuclei and their eventual size. When a nucleus reaches a certain critical radius (r^*), the system thermodynamically decreases its critical excess free energy (ΔGr^*) through growth of larger clusters. Conversely, nuclei with a radius smaller than their critical value can readily decompose, with the new nuclei composed of the agglomeration of smaller nuclei. The authors successfully synthesized denary HEAs without any phase

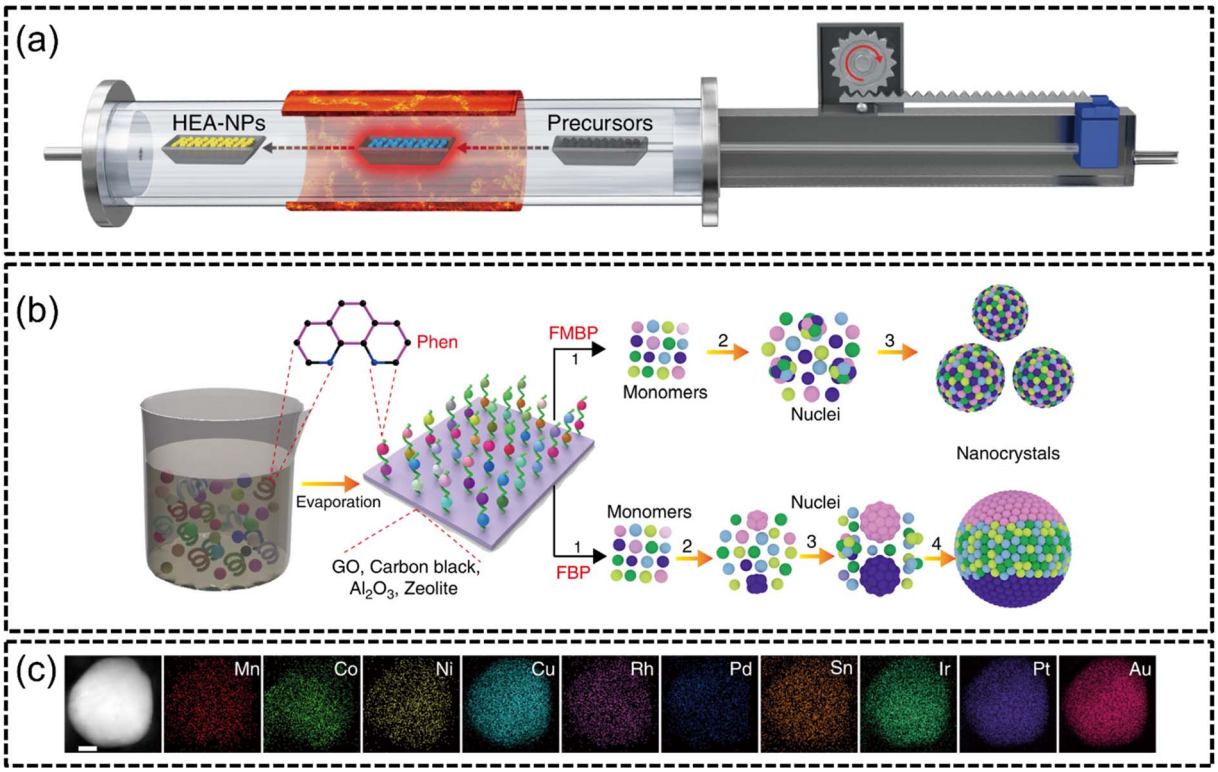

Fig. 6 FMBP synthesis from the work of Gao *et al.*, (a) illustration of the FMBP experimental setup to synthesize HEA NPs from precursors, (b) schematics for the synthesis of HEA NPs which are homogeneous when synthesized *via* FMBP, and phase-separated when synthesized *via* fixed bed pyrolysis (FBP), and (c) STEM-EDX elemental mapping of MnCoNiCuRhPdSnIrPtAu constituents. The scale bar is 10 nm. Reproduced with permission.[105] Copyright Springer Nature 2020.

separation *via* FMBP, as shown in Fig. 6(c). Since the FMBP process provided ample amounts of heat at 923 K, the temperature required to achieve a small r^* of 0.313 nm with the corresponding ΔGr^* was very much achievable. Furthermore, the authors suggested that the short time span of heating was a reason for the creation of smaller sized particles since only little energy is required for nucleation. The HER testing of FeCoPdIrPt on graphene oxide (FeCoPdIrPt@GO) produced an excellent overpotential of only 42 mV to achieve a current density of 10 mA cm^{-2} with an excellent stability at 150 hours.

It should be noted that the FMBP technique, although novel, has unfortunately not seen much popularity compared to other synthesis methods likely due to the tediousness of the setup and high energy requirements. From this, it is yet unclear whether this technique is advantageous to electrocatalytic experiments due to a lack of research, although the versatility of this technique in creating novel multi-component HEAs has been demonstrated.

5.3. Laser-based synthesis methods

Laser metallurgy is an up-and-coming facile synthesis technique pivoting on the use of laser technology to synthesize HEA nanostructures. Approaches such as laser ablation, pulsed laser deposition (PLD) and laser irradiation synthesis have recently been adopted to synthesize HEA NPs.

5.3.1. Laser ablation synthesis. Laser ablation, in the context of HEA NP synthesis, refers to the process of removing a material from a solid surface by laser irradiation, whereby the impacted material, usually a bulk HEA target, vaporizes and is subsequently collected as nanoparticles. This synthesis method is advantageous as it is extremely facile while being able to create multi-component HEAs similar to CTS. The process requires the use of a high-powered laser which, arguably, is less energy intensive than CTS but can create the same HEA nanocatalyst products. Waag *et al.* in 2019 (ref. [106]) investigated the use of laser ablation in the synthesis of CoCrFeMnNi HEA NPs using a picosecond-pulsed laser, with the process depicted in Fig. 7(a)–(c). A solid CoCrFeNiMn ablation target was first prepared through heat treatments and the pressing of individual micropowders of each single metal to form a sheet. Then, the sheet was immersed in ethanol or water and subjected to laser ablation, as in Fig. 7(a). The authors explained that the laser beam, with sufficient energy flux, formed a plume and subsequently a cavitation bubble by the ablation of hot atoms, ions, and clusters directly from the bulk HEA target, as in Fig. 7(b). This caused the mixing of the metal liquid vapours, with subsequent fast cooling occurring almost immediately after. The vapours eventually condensed into ultrasmall HEA NPs of sizes less than 5 nm with a uniform size distribution, as in Fig. 7(c). Analysis of non-ablated areas revealed no formation of HEA NPs as revealed in STEM-EDX analysis in Fig. 7(d)–(f) where HEA NPs were only formed through laser ablation of selected areas. The resulting HEA NPs were then loaded onto carbon black and subjected to the OER in 0.1 M NaOH. The

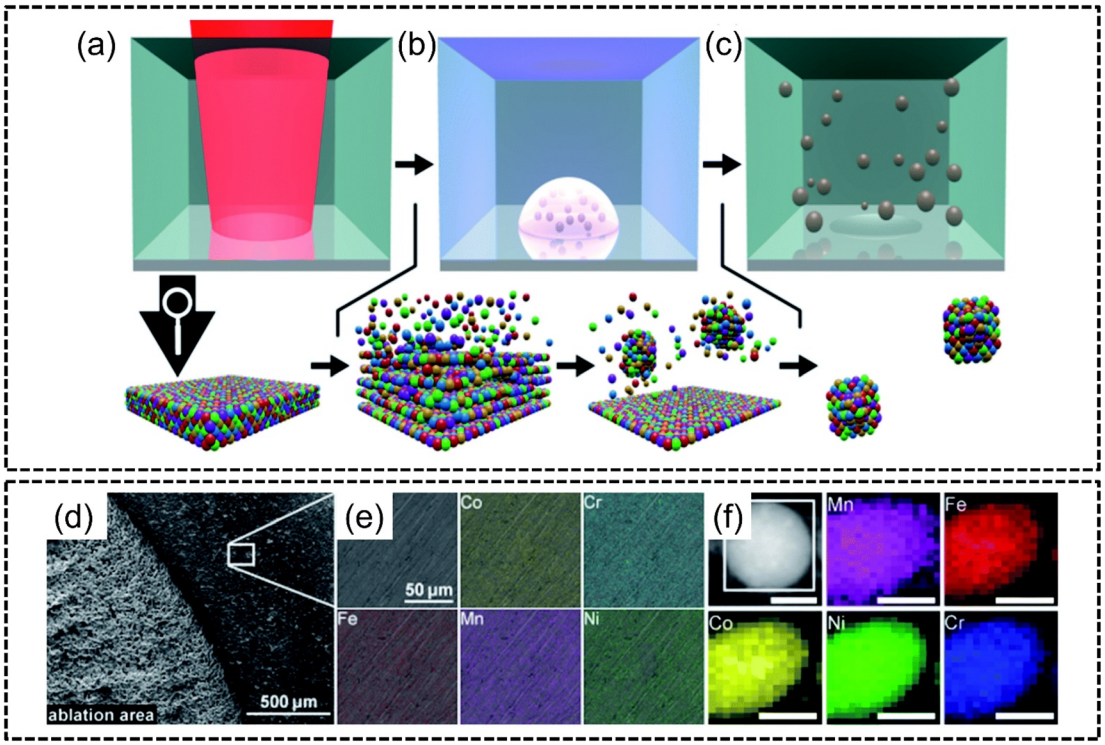

Fig. 7 Laser ablation synthesis from the work of Waag *et al.*, (a–c) schematic diagrams of the laser ablation process, (a) ultrashort-pulsed laser irradiation of bulk CoCrFeMnNi HEA, (b) formation of a plume *via* atomisation or ionization of the bulk target with the subsequent nucleation of ablated material in the gaseous phase of the liquid, and (c) formation of colloidal HEA NPs stabilized in ethanol; (d) SEM image of ablated and non-ablated areas, (e) EDX analysis of a non-ablated area with elemental mapping of Co, Cr, Fe, Mn and Ni for a single nanoparticle, and (f) STEM-EDX elemental mappings of a single CoCrFeMnNi nanoparticle. The scale bar is 25 nm. Reproduced with permission.[106] Copyright Royal Society of Chemistry 2019.

authors reported a mass activity of 0.104 A mg^{-1} for water which was higher than the reported activities of other catalysts synthesized using similar materials. Furthermore, the HEA NP catalyst was shown to be catalytically stable based on small deviations in OER performance. In terms of phase stability, the HEA was found to be stable with no separation of elements as shown in Fig. 7(f). The authors emphasized that this method is reproducible, is industrially scalable, and held much potential for materials discovery for other noble metal-free systems. Unlike many other synthesis methods, the entire laser ablation process was extremely fast with the use of a picosecond-pulsed laser.

In a more recent study by Johny *et al.*,[127] this process has similarly been used to create effective bifunctional CrCoFeNiMn and CrCoFeNiMnMo high entropy metallic glasses (HEMGs) *via* laser ablation for the OER and ORR, illustrating its versatility in HEA NP synthesis. However, the process is likely restricted to smaller scales considering a small ablation target was used for the studies as described above, such as the 20 × 20 × 2 mm target by Waag *et al.*[106] Furthermore, the pre-preparation of HEA bulk targets may be considered a bottleneck in the synthesis process where a one-pot synthesis method is often preferred.

5.3.2. Pulsed laser deposition synthesis. PLD is another similar synthesis method involving the use of a high-powered pulsed laser to synthesize HEA NPs. As a type of physical vapour deposition (PVD) technique, the PLD method employs the use of a strong pulsed laser to instantaneously vaporize a target material commonly in an ultra-high vacuum inert environment. Similar to laser ablation, the effectiveness of PLD hinges much on the absorption of laser energy on the target surface and the subsequent interaction with the surface material, plasma dynamics and plume formation and the final homogeneous deposition of the material on the substrate surface. The process is also extremely fast and the properties of the resulting HEA, such as the size, dispersity, composition, and morphology, can be controlled by varying the laser parameters.

In 2018, Cropper[108] for instance, illustrated the use of PLD to deposit AlCrFeCoNiCu HEA thin films onto borosilicate glass substrates. The author reported a mix of FCC and body centered cubic (BCC) structures in which increasing deposition temperatures diminished the resulting peak intensities in XRD. The HEA thin films were reported to be 35 nm and the FCC crystallites had similar sizes to the film thickness while BCC crystallites were larger depending on deposition temperature. This study demonstrated the success of PLD in synthesizing HEA nanostructures, although it did not demonstrate its performance in electrocatalytic applications. Recently, Chen *et al.* in 2022 (ref. [109]) demonstrated the use of PLD to synthesize CrMnFeCoNi thin films on carbon cloth and nickel foam substrates for the OER. The authors reported a low overpotential of 315 mV and 287 mV to achieve a current density of 10 mA cm^{-2} for this HEA on carbon cloth and nickel foam

respectively. Through periodic electrochemical redox for 500 cycles using electrochemical cyclic voltammetry (CV), the authors reported that this complementary strategy enabled redissolution and redeposition of surface metals. This, in turn, resulted in beneficial stability effects as the HEA exhibited excellent stabilities for 300 h and 360 h for carbon cloth and nickel foam substrates respectively. Interestingly, the authors also employed the use of a magnetic field to further improve the OER kinetics through spin polarization effects. Although PLD is an extremely facile way of synthesis, a limitation, similar to laser ablation synthesis, is likely the ability to create larger scale electrodes for industrial applications which has not been reported yet to the best of our knowledge.

5.3.3. Laser irradiation synthesis. Laser irradiation synthesis involves the use of a high-powered pulsed laser to nearly instantly heat and subsequently cool metallic precursors to synthesized multi-component HEAs.[110] The entire irradiation process is usually reported on the scale of milliseconds, which makes this method of synthesis outstandingly facile. Several recent studies have explored the use of laser metallurgy to synthesize multimetallic nanomaterials for a range of applications including circuit patterning,[111,112] the HER and the OER.[113,114]

Yan *et al.* in 2022 (ref. [110]) employed the use of a high-powered nanosecond pulse laser to synthesize binary FeNi or FeCo, ternary FeCoNi, and quinary MnFeCoNiCu or MnFeCoNiZn HEAs for the OER from metal–organic frameworks (MOFs). The authors reported that the operation of the laser was extremely fast and the eventual HEA NPs formed had a narrow size distribution. The FeNi binary alloy nanoparticles showed a particle size distribution of approximately 7 nm and demonstrated good results for the OER with an overpotential of 282 mV at a current density of 10 mA cm^{-2}, which was better than the performance of a conventional RuO_2 catalyst with 328 mV at the same current density. Furthermore, *via* electrochemical impedance spectroscopy (EIS), the FeNi alloy showed the smallest charge transfer resistance compared to the RuO_2 benchmark and other synthesized HEAs and multimetallic alloys. Additionally, the authors reported no phase separation between the transition metal elements in the HEA. It was established that the creation of multi-component HEAs was enabled because of the localized reductive atmosphere created around laser irradiation spots, thereby forming the HEA. Phase segregation was also avoided because of the instant heating and cooling using the laser. The authors fixed the parameters of the laser to have a fixed laser wavelength, pulse energy, laser frequency, beam size, and scribing speed. However, the effects of these parameters on HEA morphology and performance were not explicitly mentioned.

Lu *et al.*[115] in the same year synthesized an FeCoNiCuPtIr bifunctional HEA *via* laser irradiation for both the HER and OER. The authors demonstrated a facile method of dripping mixed metal precursor solution onto multi-wall carbon nanotubes (MWCNTs) and subjecting it to ultra-fast laser impact, as shown in Fig. 8(a). The effect was the decomposition of the metal precursors which formed uniform size nanoparticles homogeneously coated onto the surfaces. They also demonstrated that laser irradiation increased the temperature to around 1600 K from room temperature in about 50 ms, which was then followed by ultra-fast cooling to room temperature, as shown in Fig. 8(b) and (c), resulting the decomposition of the precursor solution and formation of HEA NPs. The sizes of the nanoparticles were controlled by adjusting the laser impact duration where longer durations formed larger sized particles due to diffusion, and *vice versa*. The authors reported that the entire synthesis process was completed in less than a millisecond with no phase separation occurring, as shown in Fig. 8(d). The HEA catalyst demonstrated excellent electrocatalytic performance with overpotentials of 21 mV at −10 mA cm^{-2} for the HER and 255 mV at 10 mA cm^{-2} for the OER, which outperformed conventional Pt/C and RuO_2 benchmarks for the respective reactions. The catalyst was also reportedly stable at 10, 20 and 30 mA cm^{-2} despite being subjected to 20 hours of catalysis. This method of synthesis was demonstrated to be extremely fast and cost-effective, although more experimentation involving industrial-scale sample sizes is likely required to ascertain its effectiveness for commercial synthesis of HEA NPs.

5.4. Dealloying synthesis methods

The process of dealloying involves the selective removal of one or more elements from a multi-component high entropy material to create nanostructured defects such as pores. Consequently, this affords the resulting porous nanostructure a greater surface-to-volume ratio with other advantageous effects including increased electrochemical surface area and therefore better performance in electrocatalytic applications. This process is also known as a top-down method of synthesis which has been widely adopted in many recent studies and has demonstrated a high degree of repeatability.

5.4.1. Chemical dealloying synthesis. In chemical dealloying, the HEA-loaded substrate is generally submerged into a chemical solution of either highly corrosive acids or alkali to selectively etch away specific elements in the HEA, particularly aluminum (Al) which is amphoteric in nature, thereby making it susceptible to gentler dealloying using alkaline etchants instead of harsher acids.[116–118] Jin *et al.*[119] demonstrated the dealloying of Al-based AlNiCoIrMo HEA NPs to achieve a resulting[119] nanoporous catalyst for water splitting applications in acidic environments. Using 0.5 M NaOH solution, the Al content in the HEA was selectively removed to realize this nanoporous structure containing ultrafine nanopores and nanoligaments. The authors achieved a good overpotential in the OER of 275 mV for 10 mA cm^{-2} which was an improvement when benchmarked against commercial Pt/C–IrO_2 catalysts. Furthermore, the final nanocatalyst product suffered no degradation despite 7000 CV cycles, indicating its surprising stability despite having defects such as nanopores. Separately, the authors also remarked that the incorporation of non-noble metals such as Mo, Cu and Cr can improve the performance of the catalyst when employed for OER applications. The authors concluded that this dealloying strategy has tremendous potential to synthesize novel HEA catalysts for both the OER and HER, plus other important reactions such as the oxygen reduction reaction (ORR).

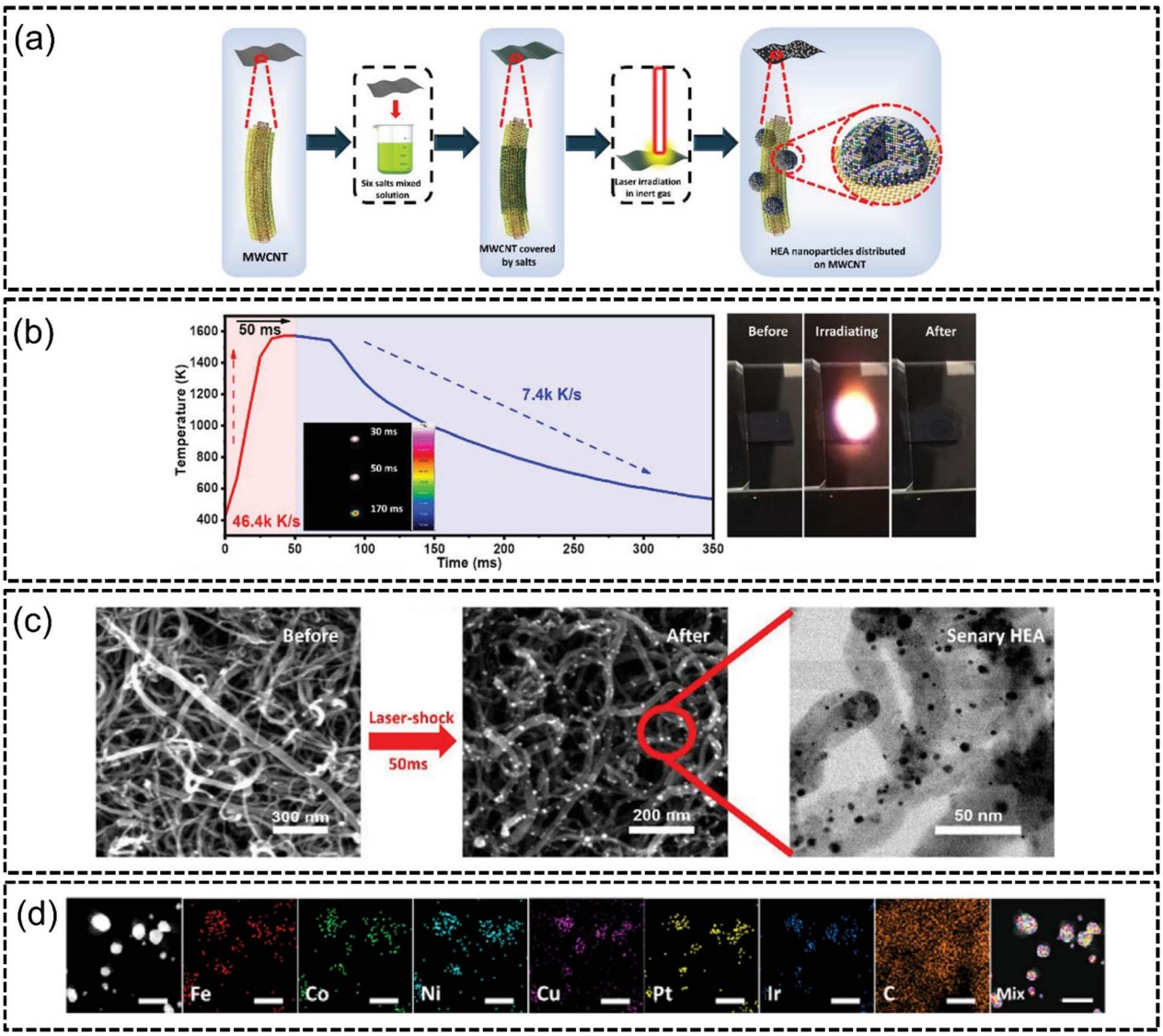

Fig. 8 Laser irradiation synthesis of FeCoNiCuPtIr HEA on MWCNTs from the work of Lu *et al.*, (a) illustration of sample preparation, (b) temperature–time measurements of the duration of laser irradiation of a specific laser spot, (c) FESEM images of salt precursors on MWCNTs before and after laser irradiation, and (d) STEM-EDX elemental mapping of the HEA elements. The scale is 10 nm. Reproduced with permission.[115] Copyright Wiley-VCH GmbH 2022.

Indeed, a few years later, the same authors above demonstrated the same dealloying strategy to synthesize HEA clusters on HEO supports where PtPdAuAgCuIrRu HEA nanoclusters were supported by AlNiCoFeCrMoTi HEO.[120] A two-step melt-spinning alloying and subsequent chemical dealloying in alkali was used, as shown in Fig. 9(a). The HEA nanoclusters had particle sizes of about 1.5–2 nm and were homogeneously dispersed with the HEO supports. Overall, the HEA cluster@HEO material was in the form of nanowires with diameters of approximately 50–100 nm which was confirmed by both SEM and TEM analyses, as shown in Fig. 9(b) and (c). Interestingly, the selected area electron diffraction analysis in the inset of Fig. 9(c) revealed that the HEO spinel structures were polycrystalline in nature. HAADF-STEM imaging confirmed that HEA nanoclusters were uniformly distributed on HEO supports as shown in Fig. 9(d). The HEA cluster@HEO also displayed excellent phase stability with no phase separation despite combining HEA clusters on HEO supports as shown in Fig. 9(e). The authors subjected this catalyst to the OER and ORR and reported a very low overpotential of 240 mV to reach a current density of 10 mA cm^{-2} for the OER, whereas conventional IrO_2 required an overpotential of 295 mV to reach the same current density. The authors described that this methodology of synthesis enabled the creation of complicated HEA@HEO nanocomposites with a high degree of tunability of components. For instance, the authors were also able to incorporate V into AlNiCoFeCrMoTi; however they found that the catalytic activity was optimized with just AlNiCoFeCrMoNi. The authors concluded that this work was pivotal in the creation of multifunctional catalysts using high entropy composites.

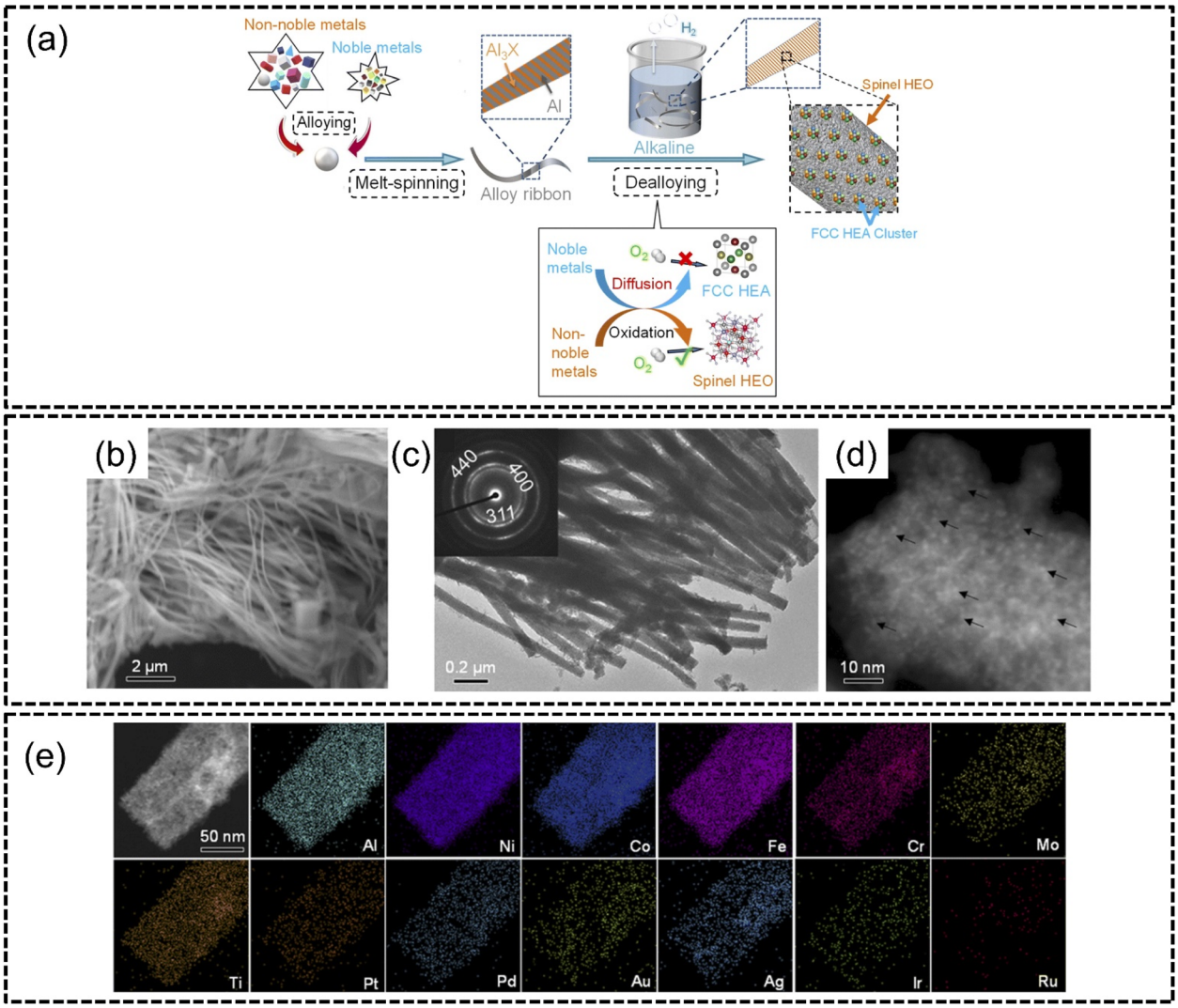

Fig. 9 Chemical dealloying synthesis from the work of Jin *et al.*, (a) schematic illustrations of the two-step alloying and dealloying of PtPdAuAgCuIrRu HEA on $(AlNiCoFeCrMoTi)_3O_4$ HEO, images of HEA cluster@HEO taken using (b) SEM, (c) TEM, (d) HAADF-STEM, and (e) STEM-EDX elemental mappings of the HEA cluster@HEO. The scale is 50 nm. Reproduced with permission.[120] Copyright Royal Society of Chemistry 2022.

5.4.2. Vapour-phase dealloying synthesis. In contrast to chemical dealloying synthesis, vapour-phase dealloying (VPD) involves the use of high temperatures to selectively evaporate elements with low melting and boiling points to create porous nanostructures for efficient HER and OER. A popular sacrificial element for this method is zinc (Zn) with a relatively low melting point (419.5 °C) and boiling point (907 °C).[121–123] Han *et al.*[122] in 2018 demonstrated this technique in the VPD of a Ni–Zn alloy ingot. Using a tube furnace with an inert atmosphere, the Ni–Zn samples were heated under pressure for different periods of time. Zn was found to be the most susceptible to sublimation under pressure and at high temperatures compared to Ge and Ni, making it suitable for sacrificial dealloying. The effect of Zn evaporation was a significant increase in porosity of the sample. The authors afford the resulting nanoporous material tremendous potential for applications such as the growth of nanoporous graphene and the anodes of Li-ion batteries. Apart from Zn, elements such as Cd, Mg, Li, Sr, Ca, Ba, Sb and Pd were identified as potential sacrificial elements by the authors.

Kwon *et al.*[124] in 2023 followed up on this finding and synthesized bifunctional ZnNiCoIrX (X = Fe, Mn) for both the OER and HER *via* the sol–gel method and subsequent VPD of Zn through a high-vacuum process in an inert atmosphere, as shown in Fig. 10(a), to obtain a nanoporous structure, as shown in Fig. 10(b) and (c). The ZnNiCoIrMn HEA was shown to have excellent phase stability with homogeneous distribution of elements in the nanoporous structure, as shown in Fig. 10(d). This HEA exhibited excellent performance for both the HER and OER with overpotentials of 50 mV for the HER at -50 mA cm^{-2} and 237 mV overpotential for the OER at 10 mA cm^{-2} which was

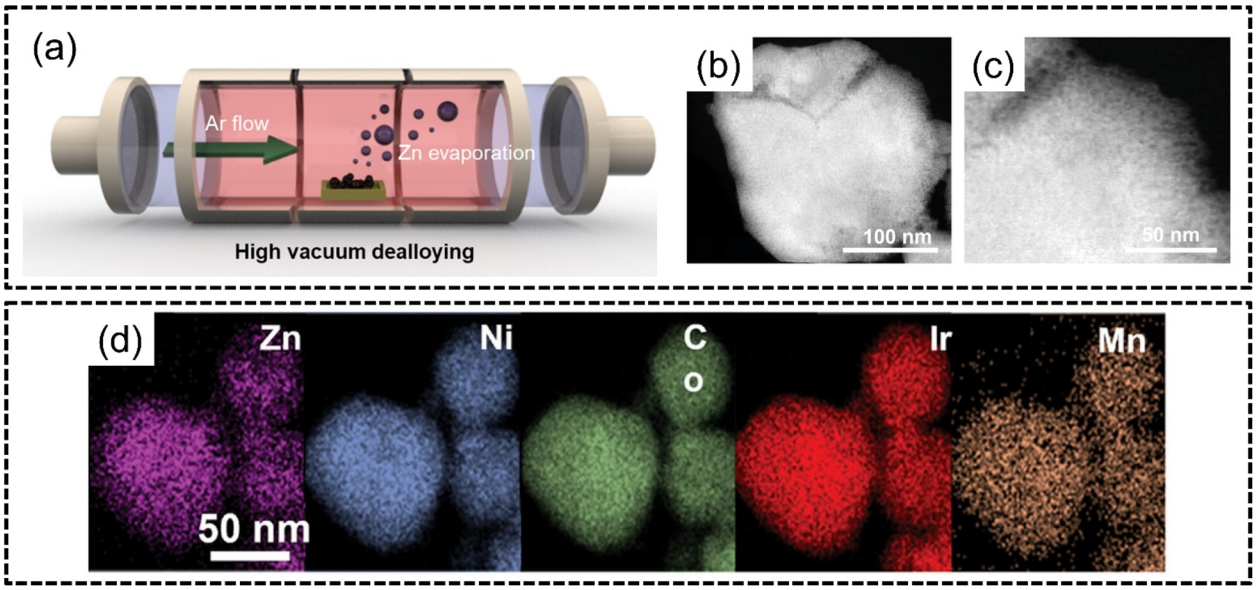

Fig. 10 Vapour phase dealloying from the work of Kwon *et al.* (a) Schematic illustration of selective Zn dealloying *via* the VPD process, and (b) and (c) STEM images, and (d) STEM-EDX elemental mapping of ZnNiCoIrMn. The scale is 50 nm. Reproduced with permission.[124] Copyright Wiley-VCH GmbH 2023.

better than those of noble metal benchmarks Pt/C and Ir/C. The authors attributed the excellent catalytic abilities to the nanoporous structure formed from VPD since the number of exposed electrocatalytic active sites per unit area increases without any modification to the intrinsic properties of the electrode. The authors further derived comparisons between VPD and conventional chemical dealloying. Although chemical dealloying can result in a loss of crystallinity which may improve catalytic activity, there will remain uncoordinated bonds which may solvate into the electrolyte solution. The ultimate effect of chemical dealloying, as the authors opine, may be a reduction in the stability of the catalyst. This catalyst also displayed remarkable durability in both acidic OER and HER even after 100 hours of continuous electrolysis, as hypothesized by the authors.

Table 2 lists several recent noble metal-free HEAs synthesized with different methods along with the crystal structure formed by the HEA, and their respective applications in catalysis.

6. Electrocatalytic performance of noble metal-free HEAs in the HER

The hydrogen evolution reaction (HER) involves the reduction of protons or water molecules to hydrogen gas, typically facilitated by a catalyst at the cathode in an electrochemical cell. The HER mechanism generally follows two main pathways: the Volmer step (proton reduction to adsorbed hydrogen) followed either by the Tafel step or the Heyrovsky step. The overall and elementary reaction equations are listed as eqn (6.1)–(6.8). At the Volmer step, the protons (acidic) or dissociated water (alkaline) molecules are adsorbed on catalyst substrates. Following the Heyrovsky step, another proton will react with the adsorbed hydrogen atom (H^*). Alternatively, at the Tafel step, two adjacent hydrogen atoms combine together to form a hydrogen molecule.

Under acidic conditions,

$$\text{Overall: } 2H^+ + 2e^- = H_2(g) \quad (6.1)$$

$$\text{Volmer: } * + H^+ + e^- = H^* \quad (6.2)$$

$$\text{Heyrovsky: } H^+ + e^- + H^* = * + H_2(g) \quad (6.3)$$

or

$$\text{Tafel: } 2H^* = * + H_2(g) \quad (6.4)$$

Under alkaline conditions, the proton comes from the dissociated water molecule.

$$\text{Overall: } 2H_2O(l) + 2e^- = 2OH^- + H_2(g) \quad (6.5)$$

$$\text{Volmer: } * + H_2O(l) + e^- = OH^- + H^* \quad (6.6)$$

$$\text{Heyrovsky: } H^+ + H_2O(l) + e^- = * + H_2(g) + OH^- \quad (6.7)$$

or

$$\text{Tafel: } 2H^* = H_2(g) \quad (6.8)$$

Standard methods of benchmarking the performance of catalysts for both the HER and OER include the linear scanning

voltammetry (LSV) analysis where the overpotential *versus* the reference hydrogen electrode (RHE) at a specific current density is reported. The corresponding Tafel slope retrieved from LSV gives crucial information about the kinetics of a reaction, where a steeper slope indicates a greater energy bandgap required for the reaction to proceed, and thus a higher overpotential is required for the reaction to proceed, and *vice versa*.

Conventional HER catalysts strongly rely on the utilization of noble metals, *e.g.*, Pt. According to the Sabatier principle, the best catalytic activity can only be achieved when the intermediate adsorption reaches equilibrium. As shown in Fig. 11(a), the overall reaction kinetics of the HER is primarily dependent on the adsorption free energy of hydrogen ($\triangle G_{H^*}$).[139,140] The advantage of Pt is the adequate adsorption strength of catalytic intermediates, by which the reaction barriers of the adsorption and desorption process are balanced. However, the surging energy demand makes it impractical for large-scale hydrogen production solely using these high-cost materials. Therefore, non-noble-metal HER catalysts have gained tremendous attraction. In spite of the challenging research process, recently many outstanding HER catalysts without noble metals have been reported. Some researchers focus on modulating the adsorption energy of non-noble metals. The coupling of multi-elements with different electronic properties of HEA catalysts is expected to fine-tune their adsorption energy. For example, Sivanantham *et al.*[137] synthesized a $V_xCuCoNiFeMn$ ($x = 0$, 0.5 and 1.0) HEA *via* a high-energy ball-milling process. Fig. 11(c) illustrates that $V_{1.0}CuCoNiFeMn$ exhibits the lowest overpotential (250 mV at -50 mA cm^{-2}, 1 M KOH). DFT calculations revealed that the incorporation of vanadium (V) significantly adjusts the electronic structure of the adjacent elements, due to the electron sharing from the high-valent V (Fig. 11(b)). As shown in Fig. 11(d) and (e), this modification resulted in a reduction in the energy barrier for water dissociation and

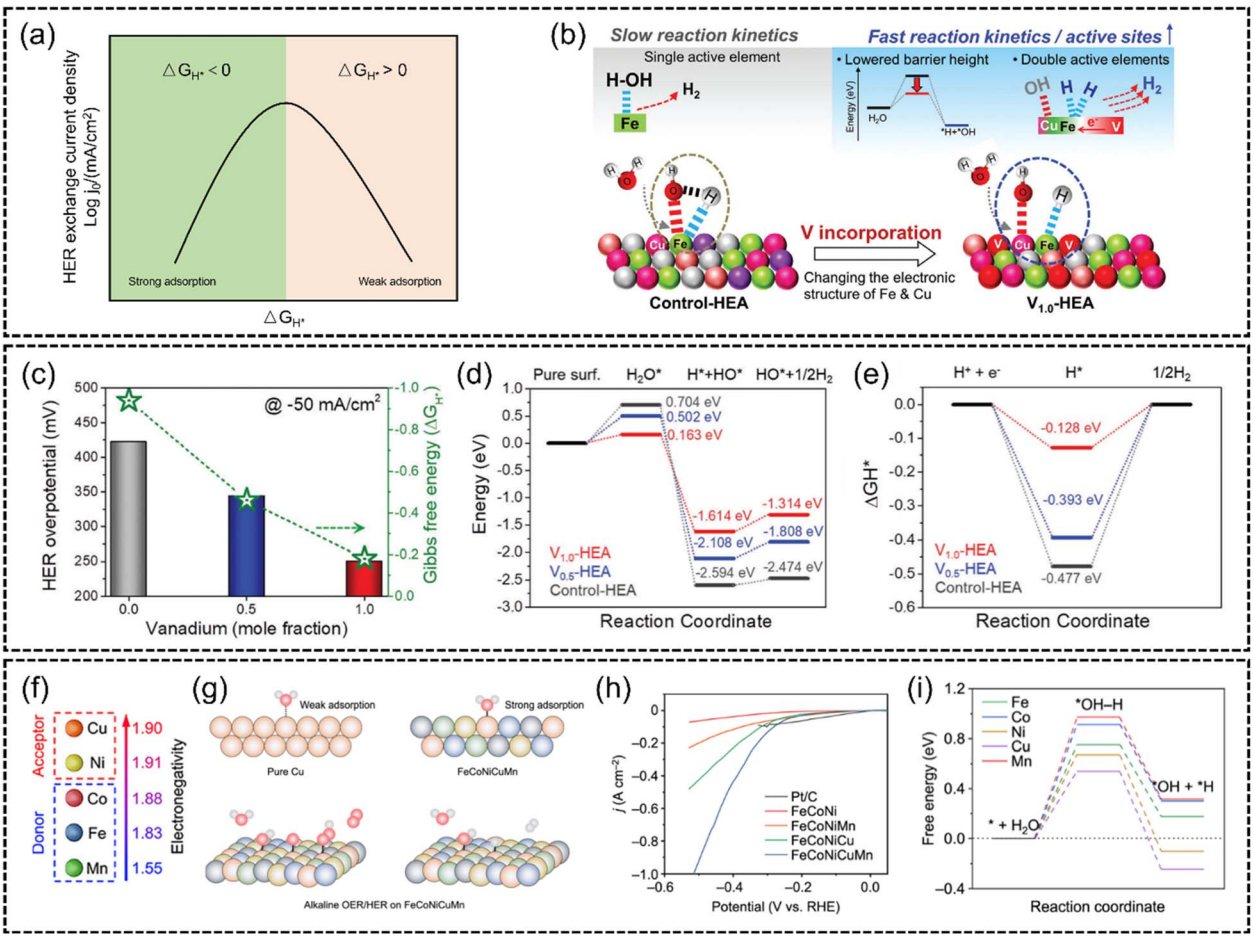

Fig. 11 (a) Schematic representation of a HER volcano plot exchange current logj_0 *versus* adsorption free energy of hydrogen ($\triangle G_{H^*}$). (b) Schematic representation of the effect of vanadium incorporation on the barrier height and active sites at the surface of $V_{1.0}$-HEA. The V incorporation adjusts the electron structure of Fe and Cu elements, lowering the water dissociation energy and increasing active sites. (c) Activity (at -50 mA cm^{-2}) *versus* Gibbs free energy (ΔG_{H^*}) relationship. (d) Reaction energy diagram of water dissociation. (e) Gibbs free energy (ΔG_{H^*}) diagram of the surface of three HEAs. Reproduced with permission.[137] Copyright 2023, Wiley-VCH GmbH. (f) A comparison of the electronegativity of the elements Cu, Ni, Co, Fe and Mn. (g) Scheme of the different adsorption strengths of intermediates on metal sites in HEAs and Cu catalysts and reaction pathways of the alkaline HER and OER at the Cu sites in the HEA NPs. (h) HER polarization curves of the FeCoNi/CNF, FeCoNiMn/CNF, FeCoNiCu/CNF, and FeCoNiCuMn HEA/CNF catalysts in 1 M KOH. (i) Gibbs free energy (ΔG_{H^*}) profiles for the HER at the Fe, Co, Ni, Cu, and Mn sites. Reproduced with permission.[141] Copyright Royal Society of Chemistry 2023.

achieves a more balanced hydrogen adsorption/desorption process, thus enhancing HER reaction kinetics. Also, Zhu *et al.*[141] introduced an innovative electronegativity-dominant approach to modulate the atomic environment. They synthesized an FeCoNiCuMn HEA by introducing low-electronegativity Mn and high-electronegativity Cu (Fig. 11(f)). Fig. 11(g) shows that the electron redistribution driven by the electronegativity difference converts the typically inactive Cu

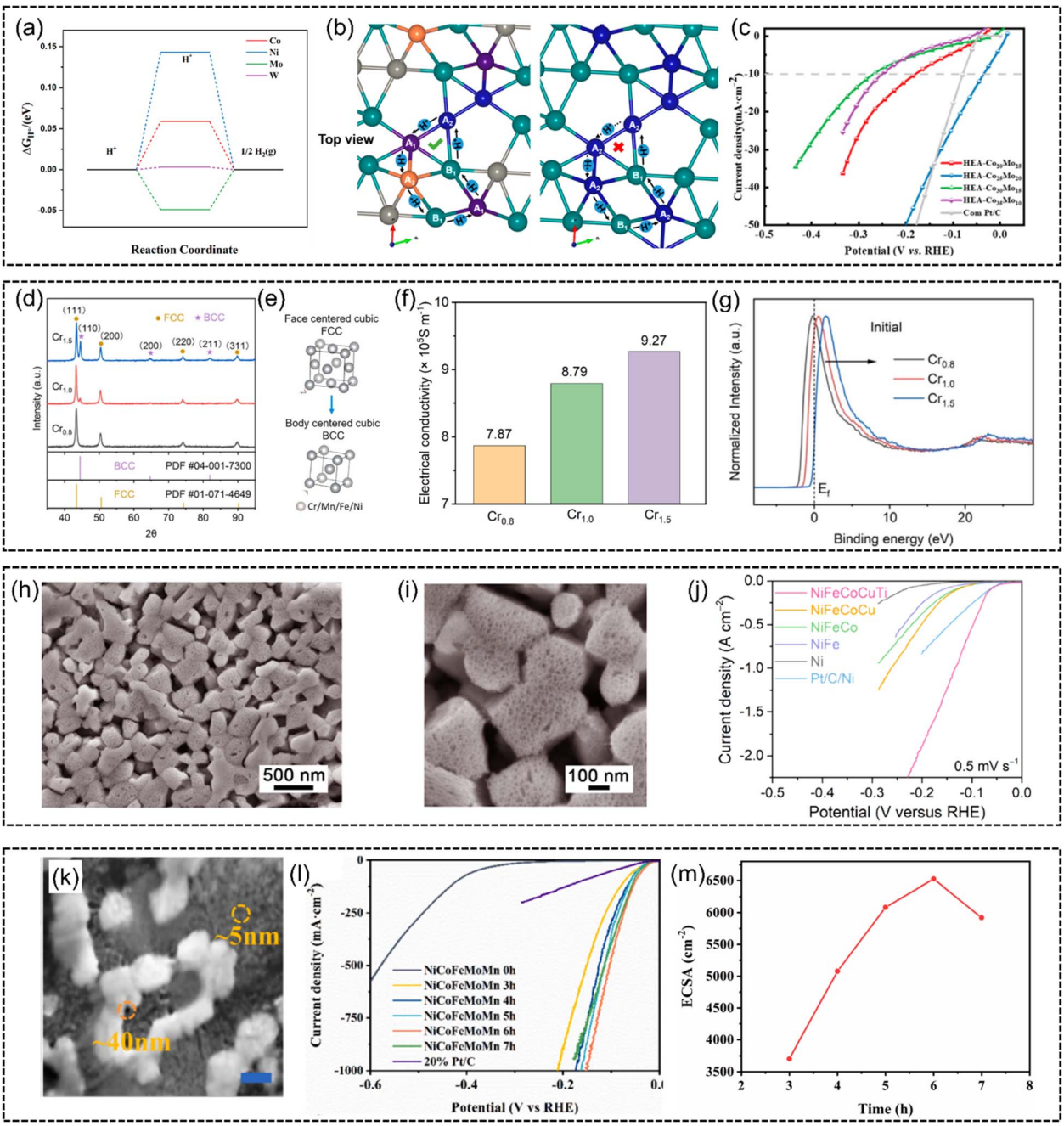

Fig. 12 (a) HER free energy of FeCoNiWMo HEA at Co, Ni, Mo, and W atomic sites. (b) Structure model and proton transport mode (top view) and (c) HER polarization curves of FeCoNiWMo HEA in 1 M KOH. Reproduced with permission.[133] Copyright 2023, American Chemical Society. (d) XRD patterns of pristine Cr_xMnFeNi (x = 0.8, 1.0, 1.5) HEAs. (e) Schematic illustration of phase transformation from the FCC phase into the BCC phase. (f) Comparison of electrical conductivity between Cr_xMnFeNi (x = 0.8, 1.0, 1.5). (g) Normalized valence band spectra (VBS) comparison of Cr_xMnFeNi (x = 0.8, 1.0, and 1.5). Reproduced with permission.[95] Copyright Elesvier 2023. (h) Low- and (i) high-magnification SEM images of a column-structured nanoporous high-entropy NiFeCoCuTi electrode fabricated by chemical dealloying in 6 M KOH solution. (j) HER polarization curves of Ti-contained nanoporous high-entropy NiFeCoCuTi, NiFeCoTi, NiFeCuTi, and NiCoCuTi electrodes, compared with NiFeCoCu without Ti. Reproduced with permission.[132] Copyright Wiley-VCH GmbH 2023. (k) SEM image of np-NiCoFeMoMn (scale bar: 100 nm). (l) HER polarization curves for nanoporous NiCoFeMoMn and commercially available Pt/C in 1 M KOH. (m) The dependence of ECSA on NiCoFeMoMn at different dealloying time intervals. Reproduced with permission.[138] Copyright Elsevier 2023.

sites to electron-rich active sites. This led to the lowest energy barriers for H_2O dissociation and H_2 production at Cu sites (Fig. 11(h) and (i)).

Besides, He *et al.*[133] proposed that the HER catalytic reaction can be completed at different sites for lower energy barriers. They proposed a rhomboidal structure of a non-noble FeCoNiWMo HEA, in which self-circulating transport pathways of protons were established to cross the potential barrier, as demonstrated in Fig. 12(b). With the disordered high-entropy state, these structures optimize the adsorption energy to facilitate the HER process (Fig. 12(a)). Significantly, a low overpotential as low as 35 mV at 10 mA cm^{-2} under alkaline conditions was achieved (Fig. 12(c)).

Wang *et al.*[95] investigated the phase-relationship of non-noble HEAs for the HER. They manipulated the phase composition in $Cr_xMnFeNi$ by increasing the Cr content (Fig. 12(d) and (e)). The FCC ($Cr_{0.8}MnFeNi$) structure was transformed into a predominant BCC phase ($Cr_{1.5}MnFeNi$). On the one hand, the BCC structure enhances catalytic activities by increasing the electric conductivity (Fig. 12(f)). On the other hand, X-ray photoelectron spectroscopy (XPS) results in Fig. 12(g) revealed that this phase engineering downshifts the d-band of the alloy system relative to the Fermi level of $Cr_{1.5}MnFeNi$ compared to $Cr_{0.8}MnFeNi$ and $Cr_{1.0}MnFeNi$. It is speculated to facilitate the electron filling of anti-bonding orbitals and weaken the bonding between HER intermediates, achieving the fine-tuning of adsorption energy.

The electrochemical active area is another factor influencing the catalytic performances, considering that a larger active area can provide more active sites for fast reaction kinetics. Thus, micro/nanostructure engineering is applied to increase the contact area of catalysts with adsorbates. For example, nanostructure engineering of carbon substrates, *e.g.*, nanosheets, carbon-based micro/nanoporous frameworks, low-dimensional support materials (graphene and carbon nanotubes), has been utilized for supporting HEA nanocatalysts.[142–146] However, in order to maintain electrical contact, insulative organic binders are needed to combine them with electrode materials. This will result in poor electrochemical performance due to their limited electron transferability and mass transportability. In this case, the electrode incorporating HEA catalysts is highly desirable. Shi *et al.*[132] reported a self-supported monolithic hybrid electrode composed of surface NiFeCoCuTi HEA on a conductive nanoporous Ni skeleton (Fig. 12(h) and (i)). Associated with column-nanostructured nanoporous architecture to expose active sites and facilitate electron transfer and H_2O/OH^- transport, the self-supported NiFeCoCuTi electrode delivers current densities of 2000 and 100 mA cm^{-2} at low overpotentials of 209 and 159 mV, respectively (Fig. 12(j)). Furthermore, Liu *et al.*[138] developed freestanding nanoporous NiCoFeMoMn foil without using electrode materials (Fig. 12(k)). This nanoporous structure was produced through an electrochemical dealloying process in a 1.0 M $(NH_4)_2SO_4$ solution. The electrochemical active surface area (ECSA) measurement demonstrates that the hierarchical porous structures increase electrochemical active area after 6 h of dealloying process (Fig. 12(m)). The (LSV) results show that it achieved an overpotential of just 150 mV at a current density of 1000 mA cm^{-2} and exhibited a low Tafel slope of 29 mV dec^{-1}.

In conclusion, the effective selection and combination of HEA elements modulate the alloy's electronic structure, electronegativity, phase composition, and surface characteristics. The integration of elements with varied electronic densities facilitates electronic structure modulation, which is crucial for reducing the energy barriers associated with water dissociation and hydrogen adsorption/desorption processes. Electronegativity engineering involves the incorporation of elements with distinct electronegative inert sites. These factors contribute to optimizing the adsorption and desorption energies of HER intermediates, enhancing catalytic efficiency and fostering the development of cost-effective, high-performance non-noble metal HER catalysts.

Table 3 lists several recent noble metal-free HEA catalysts for the HER, including the reported overpotentials at specified current densities, the Tafel slopes and the comparisons with conventional noble metal benchmarks.

Table 3 The performance of recent noble metal-free HEA catalysts for the HER

Material	Current density (mA cm^{-2})	Overpotential (mV)	Tafel slope (mV dec^{-1})	Electrolyte	Benchmark overpotential	Reference
FeCoNiAlTi	10	88.2	40.1	1.0 M KOH	Pt sheet: 145 mV	131
NiFeMoCoCr	10	107	41	0.5 M H_2SO4	Pt: ~6 mV	99
		172	66	1.0 M KOH	Pt: ~8 mV	
FeCoNiWMo	10	85	31	0.5 M H_2SO4	Pt/C: 73 mV	133
		35	31	1.0 M KOH	Pt/C: 53 mV	
NiFeCoCuTi	1000	134	43	1 M KOH	Pt/Ni/C: 134 mV at 0.43 mA cm^{-2}	147
	100	159	50	1 M PBS	Pt/Ni/C: 159 mV at 65 mA cm^{-2}	
$V_{1.0}$FeCoNiCuMn	50	250	148	1 M KOH	Pt (20%)/C: 207 mV	137
CuAlNiMoFe	100	56	60	1 M KOH	Pt/C/Cu: 232 mV	125
	10	23	50	1 M PBS	Pt/C/Cu: 23 mV	
NiCoFeMoMn	10	14	29	1 M KOH	Pt/C: 32 mV	138
FeCoNiCuMn	100	281	53	1 M KOH	Pt/C: 302 mV	141
$Cr_{1.5}$MnFeNi	30	~350	—	1 M KOH	Pt foil: ~20 mV	95
FeCoNiCu	10	155	167.8	1 M KOH	Pt/C: ~4 mV	115

7. Electrocatalytic performance of noble metal-free HEAs in the OER

The OER mechanism is a crucial process in water-splitting applications and even other electrocatalytic processes such as carbon dioxide reduction and metal–air batteries. Conventionally, the OER is defined using a four-step proton transfer process also known as the adsorbate evolution mechanism (AEM) which is regarded as thermodynamically challenging with sluggish kinetics, whereby large overpotentials are required to drive the transfer of electrons.[148,149] The use of a suitable catalyst is thus necessary to circumvent this issue. Yet, despite advances in research, this problem is an ongoing major roadblock in recent research and remains an inhibitor of commercialization. It is thus crucial to understand the fundamental mechanisms behind the OER. The AEM in an alkaline medium can be described by eqn (7.1)–(7.4):[150–152]

$$* + OH^- = OH^* + e^- \quad (7.1)$$

$$OH^* + OH^- = O^* + H_2O(l) + e^- \quad (7.2)$$

$$O^* + OH^- = OOH^* + e^- \quad (7.3)$$

$$OOH^* + OH^- = * + H_2O(l) + O_2(g) + e^- \quad (7.4)$$

where * represents a surface active site on the HEA catalyst and *O, *OH, and *OOH represent the respective adsorbate species adsorbed onto these specific active sites.

Essentially from eqn (7.1)–(7.4), the overall water oxidation reaction can be described in eqn (7.5):

$$4OH^- = O_2(g) + H_2O(l) + 4e^- \quad (7.5)$$

The first step in eqn (7.1) describes the adsorption of the OH^- ion on active sites on the HEA catalyst surface, which are typically vacancies which may arise from defects such as kinks or stacking faults.[153–155] In this step, *OH is formed. Then, in eqn (7.2), proton and electron couplings occur. Eqn (7.3)–(7.5) describe the subsequent events where *O reacts with a separate H_2O molecule and forms *OOH which further becomes oxidized into O_2 while the initial active site is restored to its original state. The AEM essentially describes Sabatier's principles, a set of DFT concepts, where the adsorption capabilities of the HEA surface should neither be too strong nor too weak to produce a good electrocatalyst.[156,157]

Recent research has pivoted around avoiding the use of noble metals to include in HEAs, which can still perform competitively in the OER compared to their noble metal counterparts. Transition metals particularly nickel (Ni), iron (Fe), and cobalt (Co) are generally included in many HEA combinations due to their relative abundance, ability to form solid solutions with other metals, and excellent performance for the OER.[158–161] Other metallic elements such as manganese (Mn), vanadium (V), and molybdenum (Mo) are often added to HEAs as enhancers of OER performance.[162–165]

Qiu *et al.*[129] synthesized AlNiCoFeX (X = Mo, Nb, Cr) noble metal-free HEAs for efficient OER *via* a chemical dealloying method. $Al_{97}Ni_{1.5}Co_{0.5}Fe_{0.5}X_{0.5}$ (X = Mo, Cr, V, Nb, *etc.*) precursor alloys were first created *via* melt-spinning and the Al content was subsequently etched with alkaline solution to obtain a nanoporous Al_3(Ni, Co, Fe, X) spinel structured HEA alloy, as shown in Fig. 13(a)–(c). The HEA was also demonstrated to have good phase stability through STEM-EDX elemental mapping shown in Fig. 13(d). In terms of performance for the OER, LSV analysis showed that AlNiFeCoMo HEA NPs exhibited the lowest overpotential of approximately 240 mV to reach 10 mA cm^{-2} in 1.0 M of KOH whereas $NiFeO_x$ and N-doped carbon catalysts required overpotentials of approximately 350 mV and 380 mV respectively for the same current density, as shown in Fig. 13(e) and (g). The Tafel slope for AlNiFeCoMo, shown in Fig. 13(f), was only 46 mV dec^{-1} which was the most gradual compared to that of the other catalysts. The HEA also outperformed the conventional RuO_2 benchmark in terms of lower overpotentials in LSV. The authors also described the effect of adding transition elements to np-AlNiCoFe where the addition of Mo was observed to have enhanced OER activity, while the addition of both Cu and/or Mo also displayed an improvement, although this improvement was not as significant as only adding Mo. Comparisons between Mo, Cr, Nb, V, Zr and Mn were also made by the authors to determine the best addition to np-AlNiCoFe. Mo, Cr and Nb were found to have greatly increased the performance of quaternary np-AlNiCoFe, and these elements were classified as 'class I' catalytic enhancers by the authors. Next, V, Zr, and Cu were determined to be weaker enhancers and thusly classified as 'class II' enhancers. Finally, Mn was determined to be the weakest enhancer element amongst all other elements tested and was classified as a 'class III' enhancer. The effect of these enhancers was tested by EIS as shown in Fig. 13(h) with the inset describing the effect of each element on activity where AlNiCoFeX (X = Mo, Nb, Cr) exhibited higher charge transfer efficiency. The authors purport that instead of the dominance of the high-entropy effect as the primary reason for good activity, miscellaneous effects such as electronic effects are the more dominant reasons for activity. The authors attributed the improved OER activity to the rapidity of interface reactions between the catalyst and electrolyte. In terms of stability, the HEA catalysts were subjected to 1000–2000 CV cycles and the AlNiCoFeMo, AlNiCoFeCu, and AlNiCoFeCuMo HEAs outperformed the rest of the samples with stable performances even after 2000 cycles without significant degradation of the nanostructure, as shown in Fig. 13(i) and (j). The authors believed that the addition of Mo and Cu could further improve the robustness of the HEA as the high-entropy effect of quinary and senary HEAs was the primary reason for the enhanced stability and concluded that modulating NiCoFe

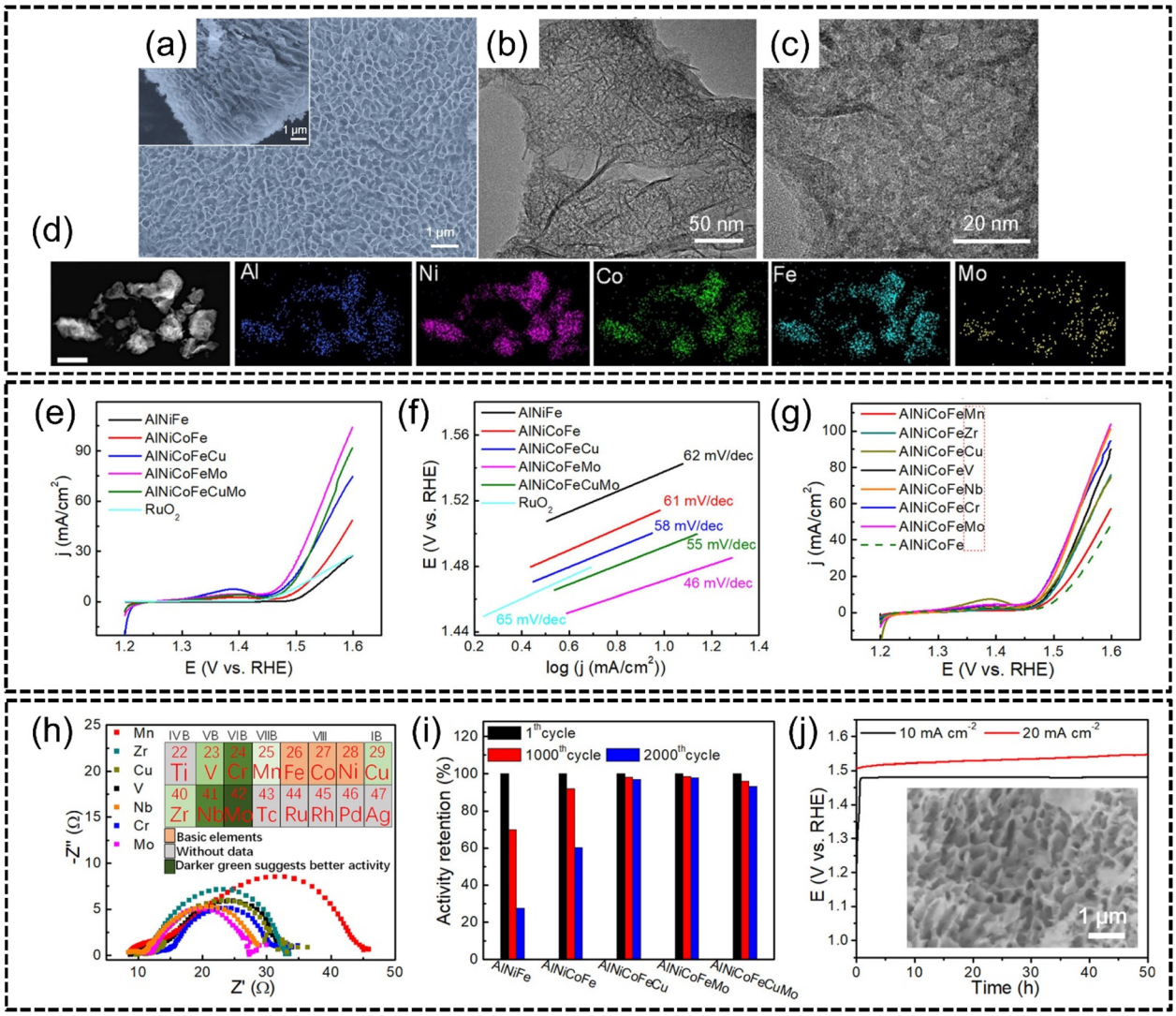

Fig. 13 The synthesis and OER performance of AlNiCoFeX (X = Mo, Nb, Cr) from the work of Qiu *et al.* Structural and morphological characterization, (a) plane-view and section view (inset) SEM images, (b) low magnification and (c) high magnification HRTEM images, and (d) STEM-EDX elemental mapping of AlNiCoFeMo nanoparticles. The scale is 150 nm. Electrochemical measurements (e), (g) LSV curves for the OER comparing different HEA combinations, (f) Tafel slopes, (h), EIS spectra with electrochemical enhancement effects of tested elements (inset), (i) potential change with time at 10 mA cm^{-2}, and (j) potential–time graph with the SEM image of AlNiCoFeMo after 50 h of testing (inset). Reproduced with permission.[129] Copyright American Chemical Society 2019.

through the incorporation of other metallic species to form HEAs was an important pathway to OER catalytic performance optimization.

He *et al.*[166] synthesized FeCoNiMoW noble metal-free HEA NPs of 35 ± 20 nm using a colloidal synthesis method in an oxygen-free atmosphere for excellent OER performance with good phase stability, as shown in Fig. 14(a) and (b). Similar to the findings in the work of Qiu *et al.*, the authors in this work reported that Mo and W helped adjust the electronic structure of the HEA while Fe, Co and especially Ni provided active sites for both the OER and ORR. Defects such as a large amount of lattice distortion, shown in Fig. 14(c) and (d), and tensile and compressive stresses were also observed within the HEA nanoparticles which were caused by the differences in the atomic radius, particularly due to the larger-sized Mo and W elements, between the constituent metal atoms and also differences in electronegativity, where Fe < Co < Ni ≪ Mo < W. The authors believed that the contributions of the severely distorted lattice and synergistic electronic coupling effects were instrumental to the excellent performance of this HEA for the OER. Based on LSV analysis, the FeCoNiMoW HEA produced an overpotential of 233 mV at 10 mA cm^{-2} and 276 mV at 100 mA cm^{-2} in 1.0 M KOH with a Tafel slope of only 36.7 mV dec^{-1}, as shown in Fig. 14(e)–(g), which outperformed an RuO_2 benchmark of 327 mV at 10 mA cm^{-2}. The authors found that the presence of 4d and 5d high valence elements, *i.e.*, Mo and W,

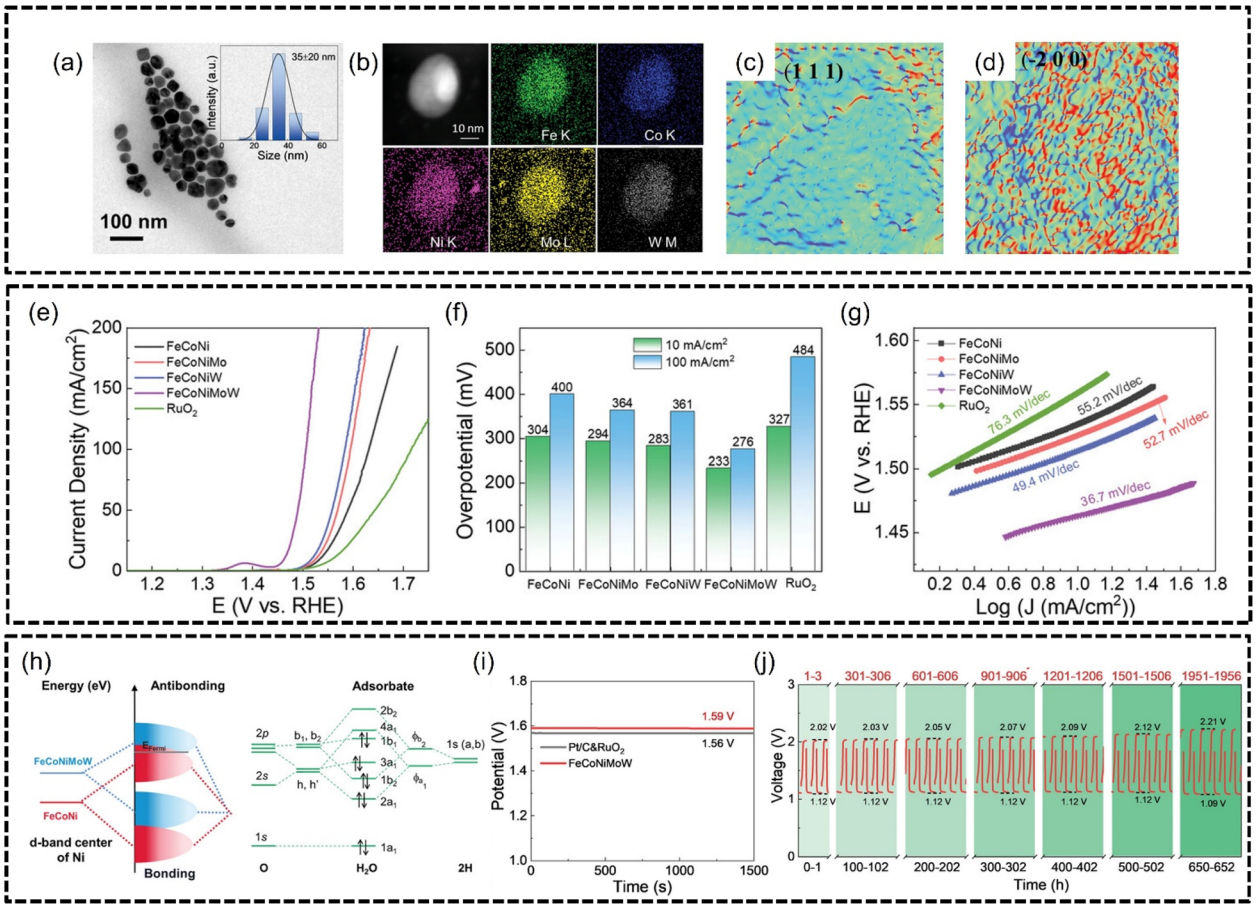

Fig. 14 FeCoNiMoW HEA characterization and OER performance based on the work of He *et al.* Structural and morphological characterization, (a) TEM image and size distribution (inset), (b) HAADF-STEM elemental mapping and (c) and (d) lattice distortion distribution maps of crystal planes (111) and (−200) zone axes of HEA based on geometric phase analysis. Electrochemical measurements, (e) LSV curves, (f) OER overpotentials at 10 and 100 mA cm^{-2}, and (g) Tafel slopes. (h) Diagram of hybridization between FeCoNi and FeCoNiMoW and O atoms of the H_2O molecule. Stability testing, (i) open-circuit potential testing, and (j) galvanostatic discharge–charge cycles at specific time periods for an FeCoNiMoW-based zinc–air battery. Reproduced with permission.[166] Copyright Wiley-VCH GmbH 2023.

affected the electronic distribution within FeCoNiMoW and the resulting HEA had the highest d-band center energy which was established using DFT calculations. Furthermore, the d orbitals of the Ni atoms were found to be hybridized with the orbitals of O atoms in H_2O in bonding states as 3d FeCoNi was combined with the 4d Mo and 5d W atoms, which explained why FeCoNiMoW performed better than FeCoNi and FeCoNiMo, as depicted in Fig. 14(h). The HEA was also tested in a zinc–air battery which exhibited an open-circuit potential of 1.59 V (which is 95.8% the theoretical limit of 1.66 V) and outperformed Pt/C and RuO_2-based batteries of 1.56 V, as shown in Fig. 14(i). The HEA anode of the zinc–air battery was also shown to have excellent stability even after 660 hours of continuous charge/discharge cycling in Fig. 14(j). The authors concluded that 4d and 5d high-valence metal modulated electronic structures were important for optimizing the adsorption ability of oxygen intermediates and the overall catalytic performance of a HEA catalyst.

Li *et al.*[167] prepared a series of FeCoNiMnX (X = Cr, Mo, W) nanoparticles *via* molten salt electrolysis of oxide mixtures coated onto nickel foam with particle sizes of approximately 5 μm, 2.5 μm and 400 nm for FeCoNiMnCr, FeCoNiMnMo and FeCoNiMnW, as shown in Fig. 15(a)–(c) respectively. Good phase stability was achieved by this synthesis method as evidenced in Fig. 15(d) where all elements are homogeneously distributed in the HEA particles. FeCoNiMnW produced the best overpotential of 243 mV at a current density of 10 mA cm^{-2} in 1.0 M of KOH with a Tafel slope of 41.5 mV dec^{-1} which was lower than FeCoNiMnMo, FeCoNiMnCr, and IrO_2/Ta_2O_5–Ti of 259 mV, 260 mV and 305 mV for the same current density, as shown in Fig. 15(e)–(g). Intriguingly, the authors reported the presence of amorphous nano-oxide arrays on the FeCoNiMnW-nickel foam electrode surface after stability testing, which was believed to provide plentiful numbers of active sites for catalysis while also helping with the desorption of oxygen, consequently resulting in better performance for the OER. FeCoNiMnW was also subjected to 100 hours of stability testing at 10 and 100 mA

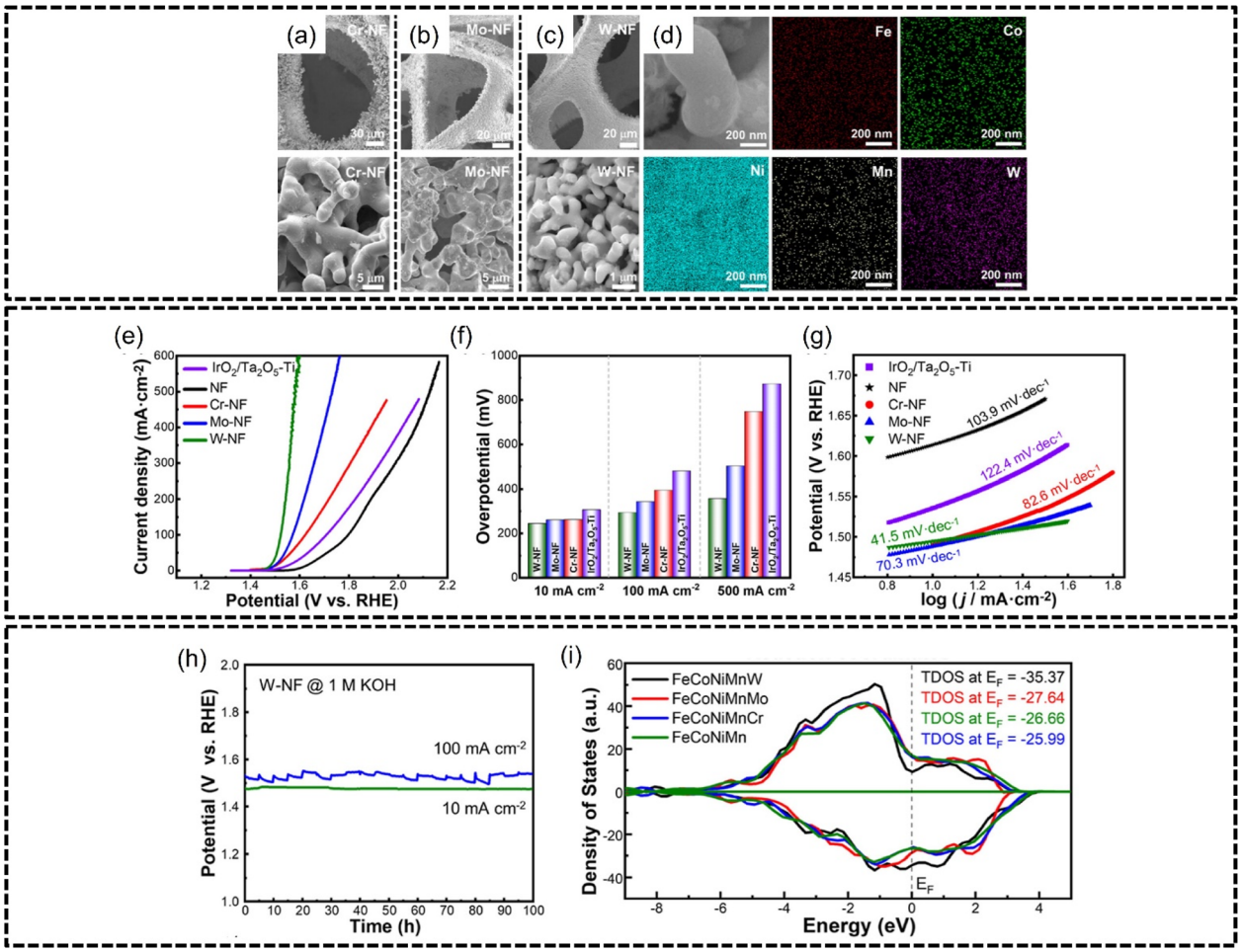

Fig. 15 FeCoNiMnW HEA characterization and OER performance based on the work of Li *et al.* Structural and morphological characterization. SEM images of (a) FeCoNiMnCr, (b) FeCoNiMnMo, and (c) FeCoNiMnW, on nickel foam, (d) EDX elemental mapping of FeCoNiMnW. Electrochemical measurements, (e) LSV curves, (f) OER overpotentials at 10, 100, and 500 mA cm^{-2}, (g) Tafel slopes, and (h) stability testing at 10 and 100 mA cm^{-2} for 100 h. (i) Total density of states plots for different electrodes. Reproduced with permission.[167] Copyright American Chemical Society 2023.

cm^{-2} and was shown to be very stable at both current densities shown in Fig. 15(h). Through DFT calculations, the authors determined that the addition of Cr, Mo and W into FeCoNiMn lessened the overpotential of the rate-determining step for the OER, thereby enabling better performance of the HEA. Interestingly, the authors discovered that the theoretical overpotential for FeCoNiMnW was close to that for HEAs containing noble metal components, which provides evidence that noble metal-free HEAs are able to theoretically perform competitively with their noble metal counterparts. Furthermore, through analysis of the total density of state values, shown in Fig. 15(i), for the various HEAs, it was found that the addition of Cr, Mo and W increased the TDOS for FeCoNiMn which enhanced the HEA performance in the OER, although the authors established the electronic influence of Ni to be an overarching factor for OER performance. Additionally, the authors synthesized FeCoNiMnW on a large-scale electrode of 40 mm × 500 mm to illustrate the scalability of this synthesis method.

In summary, it is pivotal to consider several aspects to ensure the optimized performance of noble metal-free HEAs for OER applications. The enhancement effects of certain transition metals, such as Mo, Cr, V and Nb, should be weighed together with the overall synergistic effect when combined with the other non-noble metals. Undoubtably, adjusting the content of these modulating elements is key to optimizing OER performance. Additionally, defect engineering that induces lattice distortion and compressive stresses *via* inclusion of larger-sized atoms is helpful to improving performance. Lastly, with the assistance of DFT, including certain metals such as W, Mo and Cr can increase the performance by optimizing thermodynamic factors such as TDOS.

Table 4 lists several recent noble metal-free HEA catalysts for the OER, including the reported overpotentials at specified current densities, the Tafel slopes and the comparisons with conventional noble metal benchmarks.

Table 4 The performance of recent noble metal-free HEAs for the OER

Material	Current density (mA cm^{-2})	Overpotential (mV)	Tafel slope (mV dec^{-1})	Electrolyte	Benchmark overpotential (mV)	Reference
FeCoNiCrNb	10	288	27.5	1.0 M KOH	RuO_2: 384	128
CuCoNiFeMn	40	680	196	1.0 M PBS	RuO_2: 730	168
FeCoNiCrMn	50	345	81.3	1.0 M KOH	RuO_2: 590	169
FeCoNiMnCu	10	280	63	1.0 M KOH	RuO_2: 265	170
CoCrFeNiMo	10	220	59	1.0 M KOH	—	136
	100	310				
MnFeCoNiCu	10	263	43	1.0 M KOH	RuO_2: 277	96
NiCoFeMoMn	10	243	37	1.0 M KOH	—	138
CoNiCuMnAl/C	10	215	35.6	1.0 M KOH	RuO_2: 272	171
FeCoNiCuMn	200	386	53	1.0 M KOH	IrO_2: higher overpotential (not stated)	141
CrMnFeCoNi	10	287	39	1.0 M KOH	—	109
CrMnFeCoNi	10	265	37.9	1.0 M KOH	RuO_2: 293	172
CrCoFeMnNiTiZn	50	251	42.3	1.0 M KOH	IrO_2: ~375	173
CoFeGaNiZn	10	370	71	1.0 M KOH	RuO_2: ~470	174
AlFeCoNiCr	10	240	52	1.0 M KOH	IrO_2: higher overpotential (not stated)	130
FeCoNiCuCr	10	330	80	1.0 M NaOH	RuO_2: ~345	175
FeCoNiCuZn	10	340	48	1.0 M KOH	IrO_2/Ta_2O_5–Ti: 360	176
NiFeCuCoCe	10	219	110	1.0 M KOH	IrO_2: higher overpotential (not stated)	177
CuCoMnNiFe	10	380	89.7	1.0 M KOH	RuO_2: 320	178
FeCoNiCrMo	100	303	—	1.0 M KOH	—	179
NiFeCuCoW	10	247.3	62.9	1.0 M KOH	IrO_2: higher overpotential (not stated)	180
MnFeCoNiCu	10	245	54	1.0 M KOH	RuO_2: 346	181

8. Conclusion and future developments

In the pursuit of producing clean energy by electrolysis using sustainable catalysts, HEA NPs are considered a promising novel material as catalysts for water-splitting applications due to their inherent four core effects, stability and tunability. Novel synthesis methods such as CTS, FMBP, laser ablation, PLD, laser irradiation and dealloying strategies are some of the facile techniques developed in recent years. Despite a conventional reliance on noble metals such as platinum and ruthenium to accelerate catalytic reactions for these applications, recent research has demonstrated that even noble metal-free HEA NP systems are as competent as their noble metal counterparts. This is enabled by an increased understanding nowadays of catalytic mechanisms that take place for specific reactions in the HER or OER. This is further benefitted by the fact that newer research on synthesis methods of HEA NPs often demonstrates more facile and simple synthesis steps compared to tedious processes of the past. The scaling up and commercialization of HEA NPs for various catalytic applications are therefore highly foreseeable soon. Nonetheless, several unanswered areas remain a concern for researchers:

(1) Materials discovery using machine learning (ML). At present, combinations of HEA components are often designed using trial-and-error methods and traditional first-principles-based DFT methods instead of predictive modelling offered by ML. Thus, the discovery of novel HEA NPs that can break existing intrinsic activity thresholds for the HER and OER remains sluggish without the aid of ML. However, newer research has been more focused on novel predictive models for HEA discovery. In essence, a development in this aspect of the design of HEAs can potentially streamline the development of novel HEA NPs, particularly for noble metal-free HEAs, which further contributes to the aim of facile synthesis and commercialization.

(2) OER activity is still significantly sluggish compared to HER activity. As aforementioned, the OER activity is a complex four-step proton transfer process requiring relatively higher energy to enable the reaction to proceed compared to the HER. Despite novel synthesis methods such as laser synthesis and vapour phase dealloying, HEA NPs utilized as catalysts for both noble metal and noble metal-free components still report sluggish OER kinetics. This could be attributed to a lack of understanding of OER mechanisms. Advances in multimodal techniques involving the combination of X-ray photoelectron spectroscopy, electron backscattered diffraction, HRTEM, and atom probe tomography can likely provide insights into the stability mechanisms of HEAs. Combining existing characterization techniques in novel ways may provide a greater understanding of the water splitting mechanisms.

(3) Long-term stability mechanisms are still not well understood by researchers. Phase and structural changes of HEA catalysts remain a core concern of researchers as these problems inhibit the commercial value of a catalyst for industrial use. Furthermore, nano-scale changes in HEA morphology are often extremely difficult to observe and study. Advances in *in situ* TEM techniques may provide insights into solving this problem as morphological and structural changes can be observed in real time during long-term stability testing.

(4) Experimentation with other metallic or non-metallic elements in HEA NPs. Currently, transition metals and noble metals are preferred constituents of HEA NPs due to their

excellent electrocatalytic abilities as detailed in the earlier sections above. However, there remains room for discovery in the use of less popular metals such as indium, tin, cesium, and others. Essentially, these metals can be hypothesized to modulate the adsorption energies of their other metallic counterparts in the HEA and, following Sabatier's principle, create an optimum HEA combination for effective HER/OER. Furthermore, even the use of non-metals such as sulfur or phosphorus may be able to improve the catalytic abilities of HEA NPs.

Author contributions

HK: writing – original draft, writing – review & editing, conceptualization, formal analysis, investigation. ZJH: writing – original draft, writing – review & editing, visualization, formal analysis, investigation. LY: writing – review & editing, validation, supervision, funding acquisition, project administration. WY: writing – review & editing, validation, supervision, funding acquisition, project administration. HYZ: writing – review & editing, validation, supervision, funding acquisition, project administration.

Conflicts of interest

There are no conflicts to declare.

Acknowledgements

This work was supported by the Youth Project of Liaoning Provincial Department of Education (No. JYTQN2023374). The authors also express their gratitude to the China Scholarship Council (CSC). This work was supported by the Ministry of Education, Singapore Tier 1 Academic Research Fund (No. 04MNP002134C150, RG79/20) and NTUitive Pte Ltd research grant (No. 041DP001308C150). The authors express their gratitude to both the Ministry of Education, Singapore, and Nanyang Technological University. This work was also supported by the A*STAR RIE2020 advanced manufacturing and engineering (AME) programmatic grant through the structural metal alloys program (SMAP, No. A18B1B0061). This work would not have been possible without the support of the A*STAR Graduate Scholarship from the A*STAR Graduate Academy, A*STAR, Singapore.

References

1 Y. Liang, W. Li, X. Wang, R. Zhou and H. Ding, *Ceram. Int.*, 2022, **48**, 2826–2832.
2 Y. Liang, S. Chen, J. Zhong, H. Ding, Z. Zhu and S. Li, *J. Sol-Gel Sci. Technol.*, 2022, **103**, 185–194.
3 Y. Liang, W. Li, B. Bei, C. Li, Z. He, X. Wang, R. Zhou, H. Ding and S. Li, *Appl. Clay Sci.*, 2023, **242**, 107044.
4 Y. Liang, S. Sun, T. Deng, H. Ding, W. Chen and Y. Chen, *Materials*, 2018, **11**, 450.
5 J. Sun, W. Zhen and C. Xue, *Appl. Surf. Sci.*, 2023, **623**, 157131.
6 Y. Liang, J. Sun, Y. Lu, M. Xiu, J. Zhang, J. Yue, W. Li, H. Ding, G. Xu, C. Xue and Y. Huang, *J. Alloys Compd.*, 2024, **980**, 173629.
7 L. Ju, M. Bie, X. Tang, J. Shang and L. Kou, *ACS Appl. Mater. Interfaces*, 2020, **12**, 29335–29343.
8 H. Eidsvg, S. Bentouba, P. Vajeeston, Y. Shivatharsiny and D. Velauthapillai, *Molecules*, 2021, **26**, 1687.
9 A. Meng, B. Cheng, H. Tan, J. Fan, C. Su and J. Yu, *Appl. Catal., B*, 2021, **289**, 120039.
10 T. Wang, L. Chen, C. Chen, M. Huang, Y. Huang, S. Liu and B. Li, *ACS Nano*, 2022, **16**, 2306–2318.
11 Q. Zhu, Y. Zhuang, H. Zhao, P. Zhan, C. Ren, C. Su, W. Ren, J. Zhang, D. Cai and P. Qin, *Chin. J. Chem. Eng.*, 2023, **54**, 180–191.
12 H. Wu, Q. Huang, Y. Shi, J. Chang and S. Lu, *Nano Res.*, 2023, **16**, 9142–9157.
13 R. Li and C. Li, *Adv. Catal.*, 2017, **60**, 1–57.
14 W. Li, X. Chu, F. Wang, Y. Dang, X. Liu, T. Ma, J. Li and C. Wang, *Appl. Catal., B*, 2022, **304**, 121000.
15 W. Fan, A. Wang, L. Wang, X. Jiang, Z. Xue, J. Li and G. Wang, *ACS Appl. Mater. Interfaces*, 2023, **15**, 13600–13608.
16 Y. Zhao, H. Zhou, X. Zhu, Y. Qu, C. Xiong, Z. Xue, Q. Zhang, X. Liu, F. Zhou, X. Mou, W. Wang, M. Chen, Y. Xiong, X. Lin, Y. Lin, W. Chen, H. Wane, Z. Jiang, L. Zheng, T. Yao, J. Dong, S. Wei, W. Huang, L. Gu, J. Luo, Y. Li and Y. Wu, *Nat. Catal.*, 2021, **4**, 134–143.
17 J. Xu, M. Zhong, N. Song, C. Wang and X. Lu, *Chin. Chem. Lett.*, 2023, **34**, 107359.
18 W. Chen, B. Wu, Y. Wang, W. Zhou, Y. Li, T. Liu, C. Xie, L. Xu, S. Du, M. Song, D. Wang, Y. Liu, Y. Li, J. Liu, Y. Zou, R. Chen, C. Chen, J. Zheng, Y. Li, J. Chen and S. Wang, *Energy Environ. Sci.*, 2021, **14**, 6428–6440.
19 X. Zheng, P. Cui, Y. Qian, G. Zhao, X. Zheng, X. Xu, Z. Cheng, Y. Liu, S. Dou and W. Sun, *Angew. Chem., Int. Ed.*, 2020, **59**, 14533–14540.
20 J. Feng, F. Lv, W. Zhang, P. Li, K. Wang, C. Yang, B. Wang, Y. Yang, J. Zhou, F. Lin, G. Wang and S. Guo, *Adv. Mater.*, 2017, **29**, 1703798.
21 A. L. Maulana, P. Chen, Z. X. Shi, Y. Yang, C. Lizandara-Pueyo, F. Seeler, H. D. Abruña, D. Muller, K. Schierle-Arndt and P. Yang, *Nano Lett.*, 2023, **23**, 6637–6644.
22 Z. Chen, X. Duan, W. Wei, S. Wang and B. Ni, *Nano Energy*, 2020, **78**, 105270.
23 S. M. Jowitt, G. M. Mudd and J. F. H. Thompson, *Commun. Earth Environ.*, 2020, **1**, 13.
24 A. Zupanc, J. Install, M. Jereb and T. Repo, *Angew. Chem., Int. Ed.*, 2023, **62**, e202214453.
25 J. Newbold, *J. Cleaner Prod.*, 2006, **14**, 248–261.
26 J. Chow, R. J. Kopp and P. R. Portney, *Science*, 2003, **302**, 1528–1531.
27 S. M. Barnett, K. I. Goldberg and J. M. Mayer, *Nat. Chem.*, 2012, **4**, 498–502.
28 R. Subbaraman, D. Tripkovic, K. C. Chang, D. Strmcnik, A. P. Paulikas, P. Hirunsit, M. Chan, J. Greeley, V. Stamenkovic and N. M. Markovic, *Nat. Mater.*, 2012, **11**, 550–557.

29 Y. Xin, S. Li, Y. Qian, W. Zhu, H. Yuan, P. Jiang, R. Guo and L. Wang, *ACS Catal.*, 2020, **10**, 11280–11306.
30 S. He, V. Somayaji, M. Wang, S. H. Lee, Z. Geng, S. Zhu, P. Novello, C. V. Varanasi and J. Liu, *Nano Res.*, 2022, **15**, 4785–4791.
31 P. Xie, Y. Yao, Z. Huang, Z. Liu, J. Zhang, T. Li, G. Wang, R. Shahbazian-Yassar, L. Hu and C. Wang, *Nat. Commun.*, 2019, **10**, 4011.
32 W. A. Saidi, W. Shadid and G. Veser, *J. Phys. Chem. Lett.*, 2021, **12**, 5185–5192.
33 X. Huang, K. Lei, Y. Mi, W. Fang and X. Li, *Molecules*, 2023, **28**, 5245.
34 S. Dhakar, A. Sharma, N. K. Katiyar, A. Parui, R. Das, A. K. Singh, C. S. Tiwary, S. Sharma and K. Biswas, *Mater. Today Energy*, 2023, **37**, 101386.
35 S. Nellaiappan, N. K. Katiyar, R. Kumar, A. Parui, K. D. Malviya, K. G. Pradeep, A. K. Singh, S. Sharma, C. S. Tiwary and K. Biswas, *ACS Catal.*, 2020, **10**, 3658–3663.
36 V. A. Mints, J. K. Pedersen, A. Bagger, J. Quinson, A. S. Anker, K. M. O. Jensen, J. Rossmeisl and M. Arenz, *ACS Catal.*, 2022, **12**, 11263–11271.
37 Y. Wang, J. Mi and Z. Wu, *Chem Catal.*, 2022, **2**, 1624–1656.
38 M. V. Kante, M. L. Weber, S. Ni, I. C. G. van den Bosch, E. van der Minne, L. Heymann, L. J. Falling, N. Gauquelin, M. Tsvetanova, D. M. Cunha, G. Koster, F. Gunkel, S. Nemsák, H. Hahn, L. V. Estrada and C. Baeumer, *ACS Nano*, 2023, **17**, 5329–5339.
39 J. Baek, M. D. Hossain, P. Mukherjee, J. H. Lee, K. T. Winther, J. Leem, Y. Jiang, W. C. Chueh, M. Bajdich and X. L. Zheng, *Nat. Commun.*, 2023, **14**, 5936.
40 S. Dong, H. Zhou, X. Hu, J. Zhang, Y. Li, W. Shang, Z. Liu, L. Wan and H. Zhao, *Int. J. Hydrogen Energy*, 2023, **48**, 18233–18244.
41 S. Dong, Q. Li, H. Hu, X. Zhang, Y. Li, K. Ye, W. Hou, J. He and H. Zhao, *Appl. Surf. Sci.*, 2023, **615**, 156413.
42 S. Barbarossa, R. Orrù, G. Cao, A. Balbo, F. Zanotto and E. Sani, *J. Alloys Compd.*, 2023, **935**, 167965.
43 J. Shen, Z. Hu, K. Chen, C. Chen, Y. Zhu and C. Li, *Mater. Today Nano*, 2023, **21**, 100282.
44 W. Yeh Jien, *Ann. Chim.: Sci. Mater.*, 2006, **31**, 633–648.
45 J.-W. Yeh, S. K. Chen, S.-J. Lin, J. Y. Gan, T. S. Chin, T.-T. Shun, C. H. Tsau and S. Y. Chang, *Adv. Eng. Mater.*, 2004, **6**, 299–303.
46 D. B. Miracle and O. N. Senkov, *Acta Mater.*, 2017, **122**, 448–511.
47 D. B. Miracle, J. D. Miller, O. N. Senkov, C. Woodward, M. D. Uchic and J. Tiley, *Entropy*, 2014, **16**, 494–525.
48 B. S. Murty, J. W. Yeh and S. Ranganathan, *High-Entropy Alloys*, 2016, pp. 13–35.
49 J. Ding, A. Inoue, Y. Han, F. Kong, S. Zhu, Z. Wang, E. Shalaan and F. Al-Marzouki, *J. Alloys Compd.*, 2017, **696**, 345–352.
50 R. Mu, Y. Wang, S. Niu, K. Sun and Z. Yang, *J. Eur. Ceram. Soc.*, 2023, **43**, 7263–7272.
51 X. Li, Y. Feng, B. Liu, D. Yi, X. Yang, W. Zhang, G. Chen, Y. Liu and P. Bai, *J. Alloys Compd.*, 2019, **788**, 485–494.
52 Y. Qin, F. Wang, X. Wang, M. Wang, W. Zhang, W. An, X. Wang, Y. Ren, X. Zheng, D. Lv and A. Ahmad, *Rare Met.*, 2021, **40**, 2354–2368.
53 P. Li, Y. Yao, W. Ouyang, Z. Liu, H. Yin and D. Wang, *J. Mater. Sci. Technol.*, 2023, **138**, 29–35.
54 P. Li, X. Wan, J. Su, W. Liu, Y. Guo, H. Yin and D. Wang, *ACS Catal.*, 2022, **12**, 11667–11674.
55 J. González-Masís, J. M. Cubero-Sesin, A. Campos-Quirós and K. Edalati, *Mater. Sci. Eng., A*, 2021, **825**, 141869.
56 Y. Li, L. Yang, Y. Liao, R. Zhao, L. Ji, R. Su, D. Xu and F. Wang, *Adv. Funct. Mater.*, 2023, **33**, 2302712.
57 C. L. P. Pavithra, S. A. Sankaranarayanan, M. Pebam, R. Janardhana, A. Singh, A. K. Rengan and S. R. Dey, *Mater. Lett.*, 2022, **312**, 131659.
58 X. Lei, Y. Wang, J. Wang, Y. Su, P. Ji, X. Liu, S. Guo, X. Wang, Q. Hu, L. Gu, Y. Zhang, R. Yang, G. Zhou and D. Su, *Small Methods*, 2023, **8**, 2300754.
59 A. Seoane, D. Farkas and X. Bai, *J. Mater. Sci.*, 2023, **58**, 8845–8861.
60 X. Li, J. Zhang, D. Cui, X. Luo and H. Wang, *Intermetallics*, 2022, **140**, 107400.
61 C. Zhang, F. Zhang, K. Jin, H. Bei, S. Chen, W. Cao, J. Zhu and D. Lv, *J. Phase Equilib. Diffus.*, 2017, **38**, 434–444.
62 K. Y. Tsai, M. H. Tsai and J. W. Yeh, *Acta Mater.*, 2013, **61**, 4887–4897.
63 E. J. Pickering and N. G. Jones, *Int. Mater. Rev.*, 2016, **61**, 183–202.
64 L. Wang, L. Zhang, X. Lu, F. Wu, X. Sun, H. Zhao and Q. Li, *Chem. Eng. J.*, 2023, **465**, 142766.
65 A. Hobhaydar, X. Wang, Y. Wang, H. Li, N. Van Tran and H. Zhu, *J. Alloys Compd.*, 2023, **966**, 171635.
66 F. Liu, R. Gao, C. Shi, L. Pan, Z. Huang, X. Zhang and J. Zou, *J. Am. Chem. Soc.*, 2023, **145**, 25252–25263.
67 J. C. Védrine, *Appl. Catal., A*, 2014, **474**, 40–50.
68 J. Chen and Y. Ji, *Chin. J. Catal.*, 2022, **43**, 2889–2897.
69 W. Cao, M. Zheng, W. Ding, X. Mao, C. Wang, W. Wang and J. Xin, *Mater. Res. Express*, 2019, **6**, 066558.
70 B. Wu, Y. Zhao, H. Ali, R. Chen, H. Chen, J. Wen, Y. Liu, L. Liu, K. Yang, L. Zhang, Z. He, Q. Yao, H. Zhang, B. Sa, C. Wen, Y. Qiu, H. Xiong, M. Lin, Y. Liu, C. Wang and H. Su, *Intermetallics*, 2022, **144**, 107489.
71 C. Lee, G. Song, M. Gao, R. Feng, P. Chen, J. Brechtl, Y. Chen, K. An, W. Guo, J. D. Poplawsky, S. Li, A. T. Samaei, W. Chen, A. Hu, H. Choo and P. K. Liaw, *Acta Mater.*, 2018, **160**, 158–172.
72 P. Thirathipviwat, S. Sato, G. Song, J. Bednarcik, K. Nielsch, J. Jung and J. Han, *Scr. Mater.*, 2022, **210**, 114470.
73 P. Thirathipviwat, S. Sato, G. Song, J. Bednarcik, K. Nielsch and J. Han, *Mater. Sci. Eng., A*, 2021, **823**, 141775.
74 C. M. Clausen, J. K. Pedersen, T. A. A. Batchelor and J. Rossmeisl, *Nano Res.*, 2022, **15**, 4775–4779.
75 F. Meng, W. Zhang, Z. Zhou, R. Sheng, A. C. P. Chuang, C. Wu, H. Huang, S. Zhang, H. Zhang, L. Zhu, L. Jiang, P. Liaw, S. Chen and Y. Tong, *Scr. Mater.*, 2021, **203**, 114104.
76 T. Wang, Y. Wang, N. Wang, S. Xu, Z. Han and Y. Wang, *Mater. Lett.*, 2021, **283**, 128817.

77 R. Li, P. Niu, T. Yuan, P. Cao, C. Chen and K. Zhou, *J. Alloys Compd.*, 2018, **746**, 125–134.
78 H. Li, Y. Han, H. Zhao, W. Qi, D. Zhang, Y. Yu, W. Cai, S. Li, J. Lai, B. Huang and L. Wang, *Nat. Commun.*, 2020, **11**, 5437.
79 S. Bhattacharjee, U. V. Waghmare and S. C. Lee, *Sci. Rep.*, 2016, **6**, 35916.
80 J. K. Norskov, F. Abild-Pedersen, F. Studt and T. Bligaard, *Proc. Natl. Acad. Sci. U. S. A.*, 2011, **108**, 937–943.
81 T. A. A. Batchelor, J. K. Pedersen, S. H. Winther, I. E. Castelli, K. W. Jacobsen and J. Rossmeisl, *Joule*, 2019, **3**, 834–845.
82 D. Kim, M. Chung, S. Kim, K. Yun, W. Cha, R. Harder and H. Kim, *Nano Lett.*, 2019, **19**, 5044–5052.
83 S. Li, X. Tang, H. Jia, H. Li, G. Xie, X. Liu, X. Lin and H. Qiu, *J. Catal.*, 2020, **383**, 164–171.
84 X. Cui, B. Zhang, C. Zeng and S. Guo, *MRS Commun.*, 2018, **8**, 1230–1235.
85 C. Li and J. B. Baek, *ACS Omega*, 2020, **5**, 31–40.
86 R. Paul, L. Zhu, H. Chen, J. Qu and L. Dai, *Adv. Mater.*, 2019, **31**, 1806403.
87 D. R. Lide, *CRC Handbook of Chemistry and Physics*, CRC Press, 2004.
88 S. Guo and C. Liu, *Prog. Nat. Sci.: Mater. Int.*, 2011, **21**, 433–446.
89 Y. Zhang, Y. Zhou, J. Lin, G. Chen and P. K. Liaw, *Adv. Eng. Mater.*, 2008, **10**, 534–538.
90 A. Amiri and R. Shahbazian-Yassar, *J. Mater. Chem. A*, 2021, **9**, 782–823.
91 S. Guo, C. Ng, J. Lu and C. Liu, *J. Appl. Phys.*, 2011, **109**, 103505.
92 Y. Yao, Z. Liu, P. Xie, Z. Huang, T. Li, D. Morris, Z. Finfrock, J. Zhou, M. Jiao, J. Gao, Y. Mao, J. Miao, P. Zhang, R. Shahbazian-Yassar, C. Wang, G. Wang and L. Hu, *Sci. Adv.*, 2020, **6**, eaaz0510.
93 K. Huang, J. Xia, Y. Lu, B. Zhang, W. Shi, X. Cao, X. Zhang, L. M. Woods, C. Han, C. J. Chen, T. Wang, J. Wu and Y. Huang, *Advanced Science*, 2023, **10**, 2300094.
94 J. Hao, Z. Zhuang, K. Cao, G. Gao, C. Wang, F. Lai, S. Lu, P. Ma, W. Dong, T. Liu, M. Du and H. Zhu, *Nat. Commun.*, 2022, **13**, 2662.
95 Y. Wang, N. Gong, G. Niu, J. Ge, X. Tan, M. Zhang, H. Liu, H. Wu, T. L. Meng, H. Xie, K. Hippalgaonkar, Z. Liu and Y. Huang, *J. Alloys Compd.*, 2023, **960**, 171039.
96 K. Huang, B. Zhang, J. Wu, T. Zhang, D. Peng, X. Cao, Z. Zhang, Z. Li and Y. Huang, *J. Mater. Chem. A*, 2020, **8**, 11938–11947.
97 V. Ponnambalam, S. J. Poon and G. J. Shiflet, *J. Mater. Res.*, 2004, **19**, 1320–1323.
98 Y. Li, S. J. Poon, G. J. Shiflet, J. Xu, D. H. Kim and J. F. Löffler, *MRS Bull.*, 2007, **32**, 624–628.
99 G. Zhang, K. Ming, J. Kang, Q. Huang, Z. Zhang, X. Zheng and X. Bi, *Electrochim. Acta*, 2018, **279**, 19–23.
100 A. A. H. Tajuddin, M. Wakisaka, T. Ohto, Y. Yu, H. Fukushima, H. Tanimoto, X. Li, Y. Misu, S. Jeong, J. Fujita, H. Tada, T. Fujita, M. Takeguchi, K. Takano, K. Matsuoka, Y. Sato and Y. Ito, *Adv. Mater.*, 2023, **35**, 2207466.
101 B. Cantor, I. T. H. Chang, P. Knight and A. J. B. Vincent, *Mater. Sci. Eng., A*, 2004, **375–377**, 213–218.
102 Y. Yao, Z. Huang, P. Xie, S. D. Lacey, R. J. Jacob, H. Xie, F. Chen, A. Nie, T. Pu, M. Rehwoldt, D. Yu, M. R. Zachariah, C. Wang, R. Shahbazian-Yassar, J. Li and L. Hu, *Science*, 2018, **359**, 1489–1494.
103 A. Abdelhafiz, B. Wang, A. R. Harutyunyan and J. Li, *Adv. Energy Mater.*, 2022, **12**, 2200742.
104 J. Y. Song, C. Kim, M. Kim, K. M. Cho, I. Gereige, W. B. Jung, H. Jeong and H. T. Jung, *Sci. Adv.*, 2021, **7**, eabk2984.
105 S. Gao, S. Hao, Z. Huang, Y. Yuan, S. Han, L. Lei, X. Zhang, R. Shahbazian-Yassar and J. Lu, *Nat. Commun.*, 2020, **11**, 2016.
106 F. Waag, Y. Li, A. R. Ziefuss, E. Bertin, M. Kamp, V. Duppel, G. Marzun, L. Kienle, S. Barcikowski and B. Gökce, *RSC Adv.*, 2019, **9**, 18547–18558.
107 Royal Society of Chemistry, *Periodic Table – Royal Society of Chemistry*, **https://www.rsc.org/periodic-table/**, (accessed 30 January 2024).
108 M. D. Cropper, *Appl. Surf. Sci.*, 2018, **455**, 153–159.
109 J. Chen, Y. Ling, X. Yu, G. Wang, L. Huang, A. He, Q. Fan, S. Qin, S. Xiang, M. Xu, Z. Han, J. Du and Q. Xu, *J. Alloys Compd.*, 2022, **929**, 167344.
110 W. Yan, H. Jiang, W. Yi, C. Zhao, Y. Xia, H. Cong, L. Tang, G. J. Cheng, J. He and H. Deng, *Mater. Chem. Front.*, 2022, **6**, 2796–2802.
111 R. Ma, H. Jiang, C. Wang, C. Zhao and H. Deng, *Chem. Commun.*, 2020, **56**, 2715–2718.
112 H. Jiang, S. Jin, C. Wang, R. Ma, Y. Song, M. Gao, X. Liu, A. Shen, G. Cheng and H. Deng, *J. Am. Chem. Soc.*, 2019, **141**, 5481–5489.
113 H. Wang, L. Chen, H. Pang, S. Kaskel and Q. Xu, *Chem. Soc. Rev.*, 2020, **49**, 1414–1448.
114 Q. Wang and D. Astruc, *Chem. Rev.*, 2020, **120**, 1438–1511.
115 Y. Lu, K. Huang, X. Cao, L. Zhang, T. Wang, D. Peng, B. Zhang, Z. Liu, J. Wu, Y. Zhang, C. Chen and Y. Huang, *Adv. Funct. Mater.*, 2022, **32**, 2110645.
116 H. Yuan, B. Kong, Z. Liu, L. Cui and X. Wang, *Chem. Commun.*, 2023, **60**, 184–187.
117 F. Zhou, Y. Zhou, Z. Zhang, P. Peng, J. Liang, H. Gao, M. Kang and J. Wang, *Chem. Eng. J.*, 2023, **477**, 146893.
118 T. Jian, W. Ma, J. Hou, J. Ma, C. Xu and H. Liu, *Nano Energy*, 2023, **118**, 108998.
119 Z. Jin, J. Lv, H. Jia, W. Liu, H. Li, Z. Chen, X. Lin, G. Xie, X. Liu, S. Sun and H. Qiu, *Small*, 2019, **15**, 1904180.
120 Z. Jin, X. Zhou, Y. Hu, X. Tang, K. Hu, K. Reddy, X. Lin and H. Qiu, *Chem. Sci.*, 2022, **13**, 12056–12064.
121 Z. Lu, F. Zhang, D. Wei, J. Han, Y. Xia, J. Jiang, M. Zhong, A. Hirata, K. Watanabe, A. Karma, J. Erlebacher and M. W. Chen, *Acta Mater.*, 2021, **212**, 116916.
122 J. Han, C. Li, Z. Lu, H. Wang, Z. Wang, K. Watanabe and M. Chen, *Acta Mater.*, 2019, **163**, 161–172.
123 O. Yakovenko, V. Sokolskii, N. Golovataya, T. Kulik, G. Cieslak and O. Roik, *Mater. Lett.*, 2023, **331**, 133486.
124 J. Kwon, S. Sun, S. Choi, K. Lee, S. Jo, K. Park, Y. K. Kim, H. B. Park, H. Y. Park, J. H. Jang, H. Han, U. Paik and T. S. Song, *Adv. Mater.*, 2023, **35**, 2300091.

125 R. Yao, Y. Zhou, H. Shi, W. Wan, Q. Zhang, L. Gu, Y. Zhu, Z. Wen, X. Lang and Q. Jiang, *Adv. Funct. Mater.*, 2021, **31**, 2009613.
126 X. Xu, Y. Du, C. Wang, Y. Guo, J. Zou, K. Zhou, Z. Zeng, Y. Liu and L. Li, *J. Alloys Compd.*, 2020, **822**, 153642.
127 J. Johny, Y. Li, M. Kamp, O. Prymak, S. Liang, T. Krekeler, M. Ritter, L. Kienle, C. Rehbock, S. Barcikowski and S. Reichenberger, *Nano Res.*, 2022, **15**, 4807–4819.
128 Z. Ding, J. Bian, S. Shuang, X. Liu, Y. Hu, C. Sun and Y. Yang, *Adv. Sustainable Syst.*, 2020, **4**, 1900105.
129 H. Qiu, G. Fang, J. Gao, Y. Wen, J. Lv, H. Li, G. Xie, X. Liu and S. Sun, *ACS Mater. Lett.*, 2019, **1**, 526–533.
130 G. Fang, J. Gao, J. Lv, H. Jia, H. Li, W. Liu, G. Xie, Z. Chen, Y. Huang, Q. Yuan, X. Liu, X. Lin, S. Sun and H. Qiu, *Appl. Catal., B*, 2020, **268**, 118431.
131 Z. Jia, T. Yang, L. Sun, Y. Zhao, W. Li, J. Luan, F. Lyu, L. Zhang, J. J. Kruzic, J. J. Kai, J. Huang, J. Lu and C. Liu, *Adv. Mater.*, 2020, **32**, 2000385.
132 H. Shi, X.-Y. Sun, S.-P. Zeng, Y. Liu, G.-P. Han, T.-H. Wang, Z. Wen, Q. Fang, X.-Y. Lang and Q. Jiang, *Small Struct.*, 2023, **4**, 2300042.
133 Y. He, X. Zhu, C. Zhang, Z. Liu, B. Cao, L. Sheng, Y. Yang, Q. Feng, N. Wang, J. Ou and Y. Xu, *ACS Sustainable Chem. Eng.*, 2023, **11**, 5055–5064.
134 T. Löffler, H. Meyer, A. Savan, P. Wilde, A. G. Manjón, Y. T. Chen, E. Ventosa, C. Scheu, A. Ludwig and W. Schuhmann, *Adv. Energy Mater.*, 2018, **8**, 1802269.
135 A. G. Manjón, T. Löffler, M. Meischein, H. Meyer, J. Lim, V. Strotkötter, W. Schuhmann, A. Ludwig and C. Scheu, *Nanoscale*, 2020, **12**, 23570–23577.
136 J. Tang, J. Xu, Z. Ye, X. Li and J. Luo, *J. Mater. Sci. Technol.*, 2021, **79**, 171–177.
137 A. Sivanantham, H. Lee, S. W. Hwang, H. U. Lee, S. B. Cho, B. Ahn and I. S. Cho, *Adv. Funct. Mater.*, 2023, **33**, 2301153.
138 H. Liu, H. Qin, J. Kang, L. Ma, G. Chen, Q. Huang, Z. Zhang, E. Liu, H. Lu, J. Li and N. Zhao, *Chem. Eng. J.*, 2022, **435**, 134898.
139 R. Parsons, *Trans. Faraday Soc.*, 1958, **54**, 1053–1063.
140 J. K. Norskov, T. Bligaard, A. Logadottir, J. R. Kitchin, J. Chen, S. Pandelov and U. Stimming, *J. Electrochem. Soc.*, 2005, **152**, J23–J26.
141 H. Zhu, S. Sun, J. Hao, Z. Zhuang, S. Zhang, T. Wang, Q. Kang, S. Lu, X. Wang, F. Lai, T. Liu, G. Gao, M. Du and D. Wang, *Energy Environ. Sci.*, 2023, **16**, 619–628.
142 R. Wang, J. Huang, X. Zhang, J. Han, Z. Zhang, T. Gao, L. Xu, S. Liu, P. Xu and B. Song, *ACS Nano*, 2022, **16**, 3593–3603.
143 Z. Yu, Y. Duan, X. Feng, X. Yu, M. Gao and S. Yu, *Adv. Mater.*, 2021, **33**, 2007100.
144 J. Wang, Y. Gao, H. Kong, J. Kim, S. Choi, F. Ciucci, Y. Hao, S. Yang, Z. Shao and J. Lim, *Chem. Soc. Rev.*, 2020, **49**, 9154–9196.
145 Y. Zhai, X. Ren, B. Wang and S. Z. Liu, *Adv. Funct. Mater.*, 2022, **32**, 2207536.
146 B. Wang, Y. Yao, X. Yu, C. Wang, C. Wu and Z. Zou, *J. Mater. Chem. A*, 2021, **9**, 19410–19438.
147 H. Shi, X. Sun, S. Zeng, Y. Liu, G. Han, T. Wang, Z. Wen, Q. Fang, X. Lang and Q. Jiang, *Small Struct.*, 2023, **4**, 2300042.
148 E. Fabbri, A. Habereder, K. Waltar, R. Kötz and T. J. Schmidt, *Catal. Sci. Technol.*, 2014, **4**, 3800–3821.
149 I. C. Man, H. Su, F. Calle-Vallejo, H. A. Hansen, J. I. Martínez, N. G. Inoglu, J. Kitchin, T. F. Jaramillo, J. K. Norskov and J. Rossmeisl, *Chemcatchem*, 2011, **3**, 1159–1165.
150 Q. Liang, G. Brocks and A. Bieberle-Hutter, *J. Phys.: Energy*, 2021, **3**, 026001.
151 X. Wang, H. Zhong, S. Xi, W. S. V. Lee and J. Xue, *Adv. Mater.*, 2022, **34**, 2107956.
152 J. Song, C. Wei, Z. Huang, C. Liu, L. Zeng, X. Wang and Z. C. J. Xu, *Chem. Soc. Rev.*, 2020, **49**, 2196–2214.
153 L. Xu, Q. Jiang, Z. Xiao, X. Li, J. Huo, S. Wang and L. Dai, *Angew. Chem., Int. Ed.*, 2016, **55**, 5277–5281.
154 D. Yan, Y. Li, J. Huo, R. Chen, L. Dai and S. Wang, *Adv. Mater.*, 2017, **29**, 1606459.
155 H. Xu, C. Wang, G. He and H. Chen, *Dalton Trans.*, 2023, **52**, 8466–8472.
156 M. Schalenbach, A. R. Zeradjanin, O. Kasian, S. Cherevko and K. J. J. Mayrhofer, *Int. J. Electrochem. Sci.*, 2018, **13**, 1173–1226.
157 S. Wang and H. Xin, *Chem*, 2019, **5**, 502–504.
158 J. He, Z. Hu, J. Zhao, P. Liu, X. Lv, W. Tian, C. Wang, S. Tan and J. Ji, *Chem. Eng. Sci.*, 2021, **243**, 116774.
159 Y. Wu, S. Ji, H. Wang, B. G. Pollet, X. Wang and R. Wang, *Appl. Surf. Sci.*, 2020, **528**, 146972.
160 Y. Lin, X. Fan, M. Huang, Z. Yang and W. Zhang, *Chem. Sci.*, 2022, **13**, 7332–7340.
161 D. Taffa, D. Balkenhohl, M. Amiri and M. Wark, *Small Struct.*, 2023, **4**, 2200263.
162 W. Wan, H. Wu, Z. Wang, G. Cai, D. Li, H. Zhong, T. Jiang, C. Jiang and F. Ren, *Appl. Surf. Sci.*, 2023, **611**, 155732.
163 S. Sen, M. Glienke, B. Yadav, M. Vaidya, K. Gururaj, K. G. Pradeep, L. Daum, B. Tas, L. Rogal, G. Wilde and S. Divinski, *Acta Mater.*, 2024, **264**, 119588.
164 M. Hu, X. Jiang, M. Dong, M. Hu and Y. Yang, *J. Mater. Res. Technol.*, 2023, **27**, 7705–7712.
165 H. Yao, L. Pan, L. Cui, J. Wang, X. Wu, H. Wang, Z. Na, D. Li and W. Li, *Appl. Surf. Sci.*, 2024, **648**, 159079.
166 R. He, L. Yang, Y. Zhang, D. Jiang, S. Lee, S. Horta, Z. Liang, X. Lu, A. O. Moghaddam, J. Li, M. Ibáñez, Y. Xu, Y. Zhou and A. Cabot, *Adv. Mater.*, 2023, **35**, 2303719.
167 P. Li, B. Wu, K. Du, Z. Liu, E. Gao, H. Yin and D. Wang, *ACS Sustainable Chem. Eng.*, 2023, **11**, 14246–14254.
168 A. Sivanantham, H. Lee, S. W. Hwang, B. Ahn and I. S. Cho, *J. Mater. Chem. A*, 2021, **9**, 16841–16851.
169 H. Li, H. Zhu, S. Sun, J. Hao, Z. Zhu, F. Xu, S. Lu, F. Duan and M. Du, *Chem. Commun.*, 2021, **57**, 10027–10030.
170 K. Huang, D. Peng, Z. Yao, J. Xia, B. Zhang, H. Liu, Z. Chen, F. Wu, J. Wu and Y. Huang, *Chem. Eng. J.*, 2021, **425**, 131533.
171 S. Wang, W. Huo, F. Fang, Z. Xie, J. Shang and J. Jiang, *Chem. Eng. J.*, 2022, **429**, 132410.

172 R. He, L. Yang, Y. Zhang, X. Wang, S. Lee, T. Zhang, L. X. Li, Z. Liang, J. Chen, J. S. Li, A. O. Moghaddam, J. Llorca, M. Ib, J. Arbiol, Y. Xu and A. Cabot, *Energy Storage Mater.*, 2023, **58**, 287–298.
173 N.-H. Ting, T. X. Nguyen, C.-H. Lee, Y.-C. Chen, C.-H. Yeh, H.-Y. T. Chen and J.-M. Ting, *Appl. Mater. Today*, 2022, **27**, 101398.
174 L. Sharma, N. K. Katiyar, A. Parui, R. Das, R. Kumar, C. S. Tiwary, A. K. Singh, A. Halder and K. Biswas, *Nano Res.*, 2022, **15**, 4799–4806.
175 R. Nandan, M. Y. Rekha, H. R. Devi, C. Srivastava and K. K. Nanda, *Chem. Commun.*, 2021, **57**, 611–614.
176 J. Huang, P. Wang, P. Li, H. Yin and D. Wang, *J. Mater. Sci. Technol.*, 2021, **93**, 110–118.
177 H. Bian, P. Qi, G. Xie, X. Liu, D. Zhang and P. Wang, *Chem. Eng. J.*, 2023, **477**, 623–630.
178 C. Madan, S. R. Jha, N. K. Katiyar, A. Singh, R. Mitra, C. S. Tiwary, K. Biswas and A. Halder, *Energy Adv.*, 2023, **2**, 2055–2068.
179 L. Yi, S. Xiao, Y. Wei, D. Li, R. Wang, S. Guo and W. Hu, *Chem. Eng. J.*, 2023, **469**, 144015.
180 H. Bian, R. Wang, K. Zhang, H. Zheng, M. Wen, Z. Li, Z. Li, G. Wang, G. Xie, X. Liu and L. Jiang, *Surf. Coat. Technol.*, 2023, **459**, 129407.
181 X. Zhao, Z. Xue, W. Chen, X. Bai, R. Shi and T. Mu, *J. Mater. Chem. A*, 2019, **7**, 26238–26242.
182 J. Zhao, N. Liao and J. Luo, *J. Mater. Chem. A*, 2023, **11**, 9682–9690.
183 L. Xi, J. Yu, H. Jiang, Z. Wei, H. Bin, J. Pu and C. Yu, *Carbon Energy*, 2023, **5**, e367.
184 Z. Wang, Q. Hong, X. Wang, H. Huang, Y. Chen and S. Li, *Acta Phys.-Chim. Sin.*, 2023, **39**, 2303028.
185 G. Zi, D. Yu, W. Tian, S. Feng, J. Pu, C. Pei, H. Bin, Y. Shi and C. Yu, *J. Energy Chem.*, 2023, **77**, 209–216.
186 K. Huang, J. Xia, Y. Lu, B. Zhang, W. Shi, X. Cao, X. Zhang, L. M. Woods, C. Han, C. Chen, T. Wang, J. Wu and Y. Huang, *Advanced Science*, 2023, **10**, 2300094.